Microstructural Evaluations of Baseline HSR/EPM Disk Alloys

Timothy P. Gabb
Glenn Research Center, Cleveland, Ohio

Anita Garg
University of Toledo, Toledo, Ohio

David L. Ellis
Glenn Research Center, Cleveland, Ohio

August 2004

The NASA STI Program Office . . . in Profile

Since its founding, NASA has been dedicated to the advancement of aeronautics and space science. The NASA Scientific and Technical Information (STI) Program Office plays a key part in helping NASA maintain this important role.

The NASA STI Program Office is operated by Langley Research Center, the Lead Center for NASA's scientific and technical information. The NASA STI Program Office provides access to the NASA STI Database, the largest collection of aeronautical and space science STI in the world. The Program Office is also NASA's institutional mechanism for disseminating the results of its research and development activities. These results are published by NASA in the NASA STI Report Series, which includes the following report types:

- TECHNICAL PUBLICATION. Reports of completed research or a major significant phase of research that present the results of NASA programs and include extensive data or theoretical analysis. Includes compilations of significant scientific and technical data and information deemed to be of continuing reference value. NASA's counterpart of peer-reviewed formal professional papers but has less stringent limitations on manuscript length and extent of graphic presentations.

- TECHNICAL MEMORANDUM. Scientific and technical findings that are preliminary or of specialized interest, e.g., quick release reports, working papers, and bibliographies that contain minimal annotation. Does not contain extensive analysis.

- CONTRACTOR REPORT. Scientific and technical findings by NASA-sponsored contractors and grantees.

- CONFERENCE PUBLICATION. Collected papers from scientific and technical conferences, symposia, seminars, or other meetings sponsored or cosponsored by NASA.

- SPECIAL PUBLICATION. Scientific, technical, or historical information from NASA programs, projects, and missions, often concerned with subjects having substantial public interest.

- TECHNICAL TRANSLATION. English-language translations of foreign scientific and technical material pertinent to NASA's mission.

Specialized services that complement the STI Program Office's diverse offerings include creating custom thesauri, building customized databases, organizing and publishing research results . . . even providing videos.

For more information about the NASA STI Program Office, see the following:

- Access the NASA STI Program Home Page at *http://www.sti.nasa.gov*

- E-mail your question via the Internet to help@sti.nasa.gov

- Fax your question to the NASA Access Help Desk at 301–621–0134

- Telephone the NASA Access Help Desk at 301–621–0390

- Write to:
  NASA Access Help Desk
  NASA Center for AeroSpace Information
  7121 Standard Drive
  Hanover, MD 21076

NASA/TM—2004-213123

Microstructural Evaluations of Baseline HSR/EPM Disk Alloys

Timothy P. Gabb
Glenn Research Center, Cleveland, Ohio

Anita Garg
University of Toledo, Toledo, Ohio

David L. Ellis
Glenn Research Center, Cleveland, Ohio

August 2004

Acknowledgments

Document History

This research was originally published internally as HSR034 in May 1996.

Available from

NASA Center for Aerospace Information	National Technical Information Service
7121 Standard Drive	5285 Port Royal Road
Hanover, MD 21076	Springfield, VA 22100

Available electronically at http://gltrs.grc.nasa.gov

Microstructural Evaluations of Baseline HSR/EPM Disk Alloys

Timothy P. Gabb
National Aeronautics and Space Administration
Glenn Research Center
Cleveland, Ohio 44135

Anita Garg
University of Toledo
Toledo, Ohio 43606

David L. Ellis
National Aeronautics and Space Administration
Glenn Research Center
Cleveland, Ohio 44135

Summary

Six alloys representing two classes of powder metallurgy nickel-based superalloys were examined by transmission electron microscopy (TEM) and phase extraction. Alloys KM4, CH98, IN-100 and 456 are based on a Ni-18Co-12Cr composition while alloys René 88 DT and SR 3 have lower Al and Co and higher Cr contents. The γ' size distributions were determined from quantitative image analysis of the TEM images. The volume fraction of γ' and carbides and the composition of the phases were determined by a combination of phase extraction and TEM. The results showed many similarities in γ' size distributions, grain boundary serrations, and grain boundary carbide frequencies between alloys KM4, CH98, 456, René 88 DT and SR 3 when heat treated to give an approximate grain size of ASTM 6. The density of grain boundary carbides in KM4 was shown to substantially increase as the grain size increased. IN-100 and 456 subjected to a serration cooling heat treatment had much more complex γ' size distributions with very large intergranular and intragranular secondary γ' as well as finer than average cooling and aging γ'. The grain boundary carbides in IN-100 were similar to the other alloys, but 456 given the serration cooling heat treatment had a more variable density of grain boundary carbides. Examination of the phases extracted from the matrix showed that there were significant differences in the phase chemistries and elemental partitioning ratios between the various alloys.

Introduction

The High Speed Civil Transport (HSCT) will require engines designed to sustain supersonic cruise at near maximum thrust for periods near two hours. This will impose severe challenges for the high pressure compressor and turbine disks. The disks will be operating at near maximum stress and temperature for nearly 2 hours for each mission. The disks need to have a life of about 5000 cycles and 9000 hot hours. These disks will be significantly larger in diameter than current disks in aerospace turbine engines due to the higher airflow requirements of the HSCT mission. The objective of the HSR/EPM compressor/turbine disk program is to develop and demonstrate a compressor/turbine disk system suitable for the high speed civil transport. The first step in this effort has been to screen current production and developmental nickel-base disk alloys using mechanical tests specific to the HSCT mission.

The objective of this paper is to evaluate and compare the microstructures of these current baseline disk alloys. Transmission electron microscopy was used to characterize the microstructure, γ' precipitate

distribution, and minor phases that form in each of these alloys. Phase extractions and bulk chemical analyses were employed to characterize and compare the proportions and chemistries of the γ, γ', carbide, and boride phases.

Materials and Procedure

Two general composition classes of disk alloys were selected for evaluation. In the first class were several alloys having about 18 wt.% Co and 12 wt.% Cr. IN-100 is a current production alloy of Pratt & Whitney (PW) in this composition class. Alloys 456 of PW and alloys KM4 and CH98 of General Electric Aircraft Engines (GEAE) are developmental alloys in this composition class. In the second class were two alloys chosen to represent disk alloys of lower (11.9 to 13 wt.%) Co and higher (12.8 to 16 wt.%) Cr. René 88 DT is a current production alloy of GE in this composition class. Alloy SR3 of GE is a developmental alloy in this class.

All disk alloys had been produced from argon atomized powder, and subsequently compacted, extruded, and forged using proprietary processes. The alloys' nominal compositions (1,2), heat treatments, and resulting grain sizes are listed in table 1. Heat treatments were chosen to selectively vary grain size, grain boundary character and carbide distribution at the grain boundaries. A subsolvus solution treatment followed by subsequent single step air cooling was employed to produce fine grain KM4 with an average grain size of ASTM 9. Supersolvus solution heat treatments followed by single step cooling treatments produced René 88 DT, KM4, CH98, SR3, and Alloy 456-FC with nominal grain sizes of ASTM 6.

A modified proprietary thermomechanical process, supersolvus solution, and single step air cooling heat treatment was employed to produce KM4 with ASTM 3 grain size. Grain boundary character was varied by introducing large serrations along the grain boundaries through heat treatment of Alloy 456-SC (Serration Cool) and IN-100. A slow cooling step was applied between the supersolvus solution temperature and a subsolvus end temperature, followed by a conventional air cool. This trans-solvus cooling step formed coarse secondary γ' within grains and at grain boundaries, to produce grain boundary serrations (3).

After solution and air cooling heat treatments, most of the alloys were given subsequent single step aging treatments at 760 to 775 °C/8 hr to stabilize the fine aging γ'. However, 456-FC and 456-SC were heat treated 815 °C/4 hr before aging at 735 °C/8 hr, to encourage nucleation, growth, and stabilization of $M_{23}C_6$ carbides along the grain boundaries. Such a stabilization heat treatment step could also be desirable in production alloys to allow the relief of residual stresses in large disk sections.

Specimens for transmission electron microscopy (TEM) were prepared normal to the loading axis of grip sections of tensile specimens and from coupons. TEM foils were thinned in a twin-jet Tenupol-3 electropolisher using a solution of 10 percent perchloric acid and 90 percent methanol cooled to 0 °C. An applied potential of 20 to 25V with a corresponding current of 10 to 15 mA produced electron transparent foils. The foils were then lightly ion milled to remove electropolishing contamination and examined in a Phillips 400T TEM operating at 120 keV. Energy dispersive spectroscopy was performed with an integrated EG&G detector. A minimum of three foils was examined from each alloy specimen. Typical representative areas were then selected for detailed evaluations. Microbeam electron diffraction (MBED) patterns, selective area diffraction (SAD) patterns, and energy dispersive X-ray (EDX) analyses were employed to determine the chemistry and crystal structure of different particles and phases. At least 5 particles were identified and measured to obtain particle size ranges.

The size and shape of the γ' precipitates were measured from dark field TEM micrographs. These micrographs were obtained using superlattice reflections with the foil oriented close to an <001> zone axis, in order to allow true projections of cooling γ' precipitates having sides oriented parallel to {010} crystallographic planes. The resulting two dimensional representation of the precipitates was measured and quantified using Jandel Scientific's Sigma Scan/Image image analysis software. The images were scanned in a minimum resolution of 300 dpi using a flatbed scanner. The resulting electronic images were manipulated to remove scanning artifacts and maximize the contrast between the precipitates and matrix. The precipitates in cleaned-up and enhanced images were measured by one of two methods. The preferred method of outlining the precipitates

was the floodfill method available in the software. A grayscale value equal to the average of the precipitate and matrix grayscale values was set in the software. The cursor was placed within the precipitate to designate the starting point. All contiguous pixels falling within the established limits were highlighted and taken to be part of the precipitate. The use of this method allowed for a consistent way to determine the edge of the precipitate.

A manual method where the edges of the precipitates were outlined using a mouse controlled cursor was used when the brightness of the image varied too greatly to allow floodfilling of the precipitates. The manual method was also employed where precipitates overlapped but were clearly distinguishable.

Carbide phase extractions were performed using a 10 ml HCl-1 g tartaric acid-90 ml methanol electrolyte. Duplicate extractions were performed in each case. The type of carbide and boride were determined using x-ray diffraction. Their lattice parameters were also calculated.

γ´ phase extractions were then performed using a 1 g ammonium sulfate-1 g citric acid-100 ml H_2O electrolyte. The extracted γ´ phase lattice parameters were determined using x-ray diffraction. Between four and eight peaks were observed for each sample. The lattice parameter associated with each peak was calculated after indexing the diffraction patterns. The lattice parameter of each peak was plotted against the corresponding value of $\cos^2\theta$ and $\cos\theta\sin\theta$ where θ is the diffraction angle for the peak, and a line was fitted to the data using the least squares regression technique. In all cases, the plot of lattice parameter versus $\cos^2\theta$ gave the lower sum of errors and was used for subsequent calculation of the lattice parameter and error limits. To calculate the lattice parameter of the samples, the line was extrapolated to $\cos^2\theta = 0$. The error limits on the lattice parameter were calculated by assigning 95 percent confidence intervals to the regression line and extrapolating the limits to $\cos^2\theta = 0$.

The compositions of the extractions were determined by inductively coupled plasma (ICP) chemical analyses. The composition of the γ phase was determined by chemical analysis of the ammonium sulfate/citric acid electrolyte immediately after the γ′ extractions were completed.

Results and Discussion

1. TEM Microstructural Evaluations

The results of TEM evaluations of all the alloys are tabulated in tables 2 and 3. γ′ precipitate sizes determined by image analyses of TEM images are compared in table 2. In table 2, coarse γ′ of 1 to 3 μm diameter which formed during the slow trans-solvus cools in 456-SC and IN-100 was defined as secondary γ′. Finer γ′ of 0.1 to 0.5 μm diameter which formed during the air cooling from solution treatments was defined as cooling γ′. Very fine γ′ of 0.01 to 0.06 μm diameter which formed during stabilization and aging heat treatments was defined as aging γ′. Minor phases observed within grains and at grain boundaries with observed size ranges are compared in table 3. Significant variability in the frequency of carbides at grain boundaries was observed in TEM evaluations of these alloys. Grain boundaries with no carbides were observed in each alloy. Other grain boundaries had a higher number of carbides. The TEM micrographs presented illustrate the characteristics of grain boundaries having the highest observed frequency of carbides in each alloy.

a. KM 4.—Typical TEM micrographs of the general microstructures including details of the cooling and aging γ′ of KM4 with grain sizes of ASTM 3, 6, and 9 are compared in figure 1. The microstructures generally consisted of cooling γ′ and aging γ′ in a γ matrix. Primary γ′ was also present in KM4 ASTM 9, due to its subsolvus solution treatment which did not dissolve all existing γ′. The cooling and aging γ′ sizes and cooling γ′ area fractions are listed in table 2, and the γ′ size distributions are compared in figure 2. The cooling and aging γ′ sizes of KM4 ASTM 3 and 9 were similar. However, both the cooling and aging γ′ sizes of ASTM 6 KM4 were larger (fig. 2(b)), for unclear reasons. The specimen blanks of these materials were cooled at the same nominal air cooling rates from solution heat treatments; however some variabilities among specimen blanks were possible. It is possible that the KM4 ASTM 6 specimen examined had a slower actual cooling rate. The

smallest cooling γ′ size of KM4 ASTM 9 could be due to its low subsolvus solution temperature, producing a smaller temperature interval of cooling γ′ coarsening during the air cooling quench than ASTM 3 and 6 materials.

The feret diameter, the diameter of a circle with an area equal to the measured area of the image of the precipitate (see appendix B), is plotted in figure 2. The feret diameter was chosen over the major axis and other indicators of size because it is shape independent. Therefore the size of irregularly shaped precipitates can be compared directly to square and circular precipitates. Twins and stacking faults were commonly observed in all samples. (Ti,Nb)C carbides and $(Mo,Cr)_3B_2$ borides were scattered within grains, and fine Al_2O_3 and ZrO_2 particles were also identified within grains. Electron diffraction patterns and qualitative EDS spectra identifying these phases are shown in figure 3.

The grain boundaries of KM4 ASTM 3, 6, and 9 are compared in figure 4. The grain boundaries predominantly contained fine discontinuous $Cr_{23}C_6$ carbides, with an occasional presence (about 5 percent by number of each) of (Ti,Nb)C carbides and $(Mo,Cr)_3B_2$ boride particles. However, the density of $Cr_{23}C_6$ particles varied directly with grain size. Fine grain ASTM 9 KM4 had very few $Cr_{23}C_6$ carbides along the grain boundaries, with bare grain boundaries often observed. Intermediate grain size ASTM 6 KM4 had a moderate loading of these particles at many grain boundaries, with obvious separations between discrete, elongated particles. However, a smaller number of grain boundaries still had few or no observed carbides. Coarse grain ASTM 3 KM4 had a very high density of carbides at a majority of the grain boundaries. Images of grain boundaries nearly parallel to the beam suggested that the carbides in ASTM 3 KM4 were continuous. However, when these boundaries were tilted roughly normal to the beam (fig. 4(a)), the $Cr_{23}C_6$ carbides were observed to be discrete and very closely spaced, with random joining of some particles. The average sizes of the occasionally observed (Ti,Nb)C and $(Mo,Cr)_3B_2$ sizes appeared comparable for the three grain sizes.

b. CH98.—CH98 can be considered a modified form of KM4, with Ta fully substituted for Nb on an atomic basis. TEM micrographs of the general microstructure of CH98 ASTM 6 are shown in figure 5. The microstructure morphology closely paralleled that of KM4 ASTM 6, and twins and stacking faults similar to those of KM4 were present. Cooling and aging γ′ sizes and cooling γ′ area fraction are listed in table 2. The size distribution of the γ′ precipitates is presented in figure 6. The average cooling γ′ size of CH98 was finer than KM4 ASTM 6 while their aging γ′ sizes were comparable. Twins and stacking faults similar to those of KM4 were present. CH98 had generally fewer MC carbides within grains than KM4. These carbides were (Ta,Ti)C rather than (Ti,Nb)C of KM4, as shown in the EDS spectrum in figure 7 and listed in table 3. This change in MC carbide composition of CH98 is consistent with the substitution of Ta in CH98 for the Nb in KM4, and the high affinity of Ta for C. CH98 had somewhat larger Al2O3 particles within the grains than KM4.

Typical grain boundaries of CH98 are shown in figure 8. The grain boundaries were very similar to that of KM4 ASTM 6 in waviness, and had comparable $Cr_{23}C_6$ carbide frequency and size, as listed in table 3. About 10 percent of the grain boundary particles were (Ta,Ti)C carbides or $(Mo,Cr)_3B_2$ borides. The similarity of grain boundary carbide frequency and morphology of CH98 and KM4 are consistent with their comparable heat treatments and carbon contents.

c. René 88 DT and SR 3.—TEM micrographs of the general microstructures of René 88 DT and SR3 are shown in figure 9. The microstructures consisted predominantly of cooling and aging γ′ in a γ matrix, with the γ′ sizes and cooling γ′ area fractions listed in table 2. The γ′ size distributions for the alloys are shown in figure 10. The average cooling and aging γ′ sizes of these two alloys were comparable to CH98. However, SR3 had strong evidence of a bimodal distribution of cooling γ′, possibly due to dendritic growth of some of the cuboidal γ′ precipitates. René 88 DT also had evidence of this cooling γ′ morphology, which may be related to chemistry-induced differences in coarsening and γ-γ′ mismatch of these two alloys in comparison to the 18Co-12Cr alloys.

René 88 DT had the lowest area fraction of cooling γ′ (35.6 percent), and SR3 had the next lowest cooling γ′ content. This is consistent with the lower Al and Co contents of these two alloys which would reduce the equilibrium γ′ content in comparison to the 18Co-12Cr alloys. The lower cooling γ′ area fraction seemed to be accompanied by a somewhat higher area fraction of aging γ′. However, the stacking of aging γ′ particles within the foil thickness did not allow measurement of aging γ′ area fractions. SR3 also had somewhat more elongated

cooling γ′ at the grain boundaries than René 88 DT, KM4-6 or CH98, possibly due to a different cooling history of the actual blank from the other alloys. Twins and stacking faults similar to those in KM4 were observed in both alloys.

EDS spectra for the carbides and borides found in René 88 DT are shown in figure 11. René 88 DT and SR3 had $(Ti,Nb)C$ carbides within the grains of similar size and frequency to KM4. W was also present in the $(Ti,Nb)C$ carbides and $(Mo,Cr)_3B_2$ borides of René 88 DT due to the presence of W in this alloy. René 88 DT had Al_2O_3 and ZrO_2 particles within grains similar to KM4. No Al_2O_3 or ZrO_2 particles were detected in SR3. Instead, fine $(Hf,Zr)O_2$ particles were distributed within the grains of SR3, as identified by the SAD and EDS patterns in figure 12. The Hf in SR3 apparently had a high affinity for oxygen during processing. Hf is known to be a strong carbide former in superalloys (6), but no Hf carbides were observed in SR3. Hf is also known to partition to the γ′ phase (4) where it is a solid solution strengthener.

Typical grain boundaries of René 88 DT and SR3 are shown in figure 13. The grain boundaries of René 88 DT looked quite similar to that of KM4 ASTM 6 and CH98 in waviness, and $Cr_{23}C_6$ carbide frequency and size (table 3). SR3 had a lower frequency of carbides at the grain boundaries than all other alloys. About 5 percent of the grain boundary particles were $(Ti,Nb)C$ carbides in SR3, but no HfC carbides or $(Hf,Zr)O_2$ oxides were detected. No $(Mo,Cr)_3B_2$ borides were detected in SR3. René 88 DT had $(Mo,Cr,W)_3 B_2$ borides.

d. IN-100.—TEM micrographs of the general microstructure of IN-100 ASTM 6 are shown in figure 14, and the γ′ size distributions are presented in figure 15. This microstructure was significantly different from that of the previously examined 18Co-12Cr alloys due to a proprietary, multistepped, trans-solvus (serration cool) heat treatment employed for IN-100. Coarse butterfly wing shaped secondary γ′ of over 1 μm width was present within the grains, while coarse, elongated secondary γ′ of up to several microns long were located along grain boundaries. This secondary γ′ presumably nucleated and coarsened predominantly during the slow trans-solvus cooling step. The arrayed dislocations visible along the γ-γ′ interfaces of the secondary γ′ precipitates (fig. 14) indicates loss of coherency with the γ matrix. The average cooling γ′ size was comparable to that of KM4-ASTM 3 and 9, CH98, and René 88 DT (table 2). However, the aging γ′ was the finest among all the alloys, possibly due to an altered aging heat treatment. Twins were sometimes observed in IN-100, but stacking faults were rarely observed. TiC carbides identified with EDS spectra such as the one shown in figure 16 were scattered within the grains, but $(Mo,Cr)_3B_2$ borides and Al_2O_3 oxides were only rarely observed.

A TEM micrograph of a typical grain boundary in IN-100 is shown in figure 17. The coarse elongated secondary γ′ particles are indicated in the figure. The waviness of IN-100 grain boundaries was primarily dictated by the coarse secondary γ′ particles there. This produced larger scale grain boundary serrations than that observed in the previous alloys. $Cr_{23}C_6$ carbides predominated along the grain boundaries, having a sized and density similar to KM4-ASTM 6, CH98, and René 88 DT. About 5 percent of the carbides were larger TiC carbides, and $(Mo,Cr)_3B_2$ borides were rarely observed.

e. Alloy 456.—TEM micrographs of the general microstructure of Alloy 456 given a multistepped serration cool (SC) heat treatment with a slow trans-solvus cooling rate is compared to that produced using a supersolvus and single step cooling heat treatment (FC) heat treatment in figure 18. The γ′ size distributions for the alloys are presented in figure 19. Alloy 456-SC had a very similar microstructure to IN-100. Coarse secondary γ′ precipitates were located within grains, yet the cooling γ′ size was the finest among the alloys. This could be associated with the lower final quench temperature of 456-SC than the other alloys, along with the presence of tungsten in this alloy. Tungsten can partition to the γ′ and slow the γ′ coarsening rate (4). Twins and stacking faults were present, and $(Ti,Nb)C$ carbides and ZrO_2 particles were also observed scattered within grains.

Alloy 456-FC had a general microstructure similar to the other ASTM 6 alloys given single step cooling heat treatments. Only cooling and aging γ′ was observed within a γ matrix, with average cooling γ′ sizes similar to these other alloys. The aging γ′ sizes of 456-SC and 456-FC were larger than all of the other alloys. This could be associated with the stabilization heat treatment applied to these alloys which could promote enhanced nucleation and growth of aging γ′. Twins and stacking faults were again commonly observed, with scattered $(Ti,Nb)C$ particles.

Typical grain boundaries of 456-SC and 456-FC are compared in figure 20. Both materials had predominant $Cr_{23}C_6$ carbides at their grain boundaries, with minor numbers (5 percent of each) of (Ti,Nb)C carbides and $(Mo,Cr,W)_3B_2$ borides. The borides in 456-SC and FC were significantly larger than in the previous alloys, often exceeding 1 μm in maximum dimension. The frequency and density of $Cr_{23}C_6$ carbides in 456-FC were comparable to that of the other air cooled ASTM 6 alloys given single step ages, excluding SR3. The frequency and density of $Cr_{23}C_6$ carbides in 456-SC were decidedly more variable than in 456-FC. On some grain boundaries, the carbide density approached that of KM4-ASTM 3. On other grain boundaries, the density approached KM4-ASTM 9. Even comparing among similar high angle grain boundaries, the density of $Cr_{23}C_6$ carbides varied considerably. Three adjoining high angle grain boundaries having clearly different carbide densities are shown in figure 21. Therefore, the 815 °C/4 hr carbide stabilization heat treatment applied to Alloy 456-FC and SC had mixed success in stabilizing the $Cr_{23}C_6$ carbide density at grain boundaries. The variations of carbide density observed in Alloy 456-SC may be associated with variations in MC carbide density along grain boundaries before heat treatment. MC carbides react with the matrix to form $Cr_{23}C_6$ along the grain boundaries during heat treatment (6). The variations could also be related to the combined effects of the slow trans-solvus cool and the carbide stabilization on $C_{23}C_6$ formation kinetics.

2. Phase Extractions

Results of carbide phase extractions are listed in tables 4 and 5. X-ray analyses of the carbide extractions detected MC carbides, but no $Cr_{23}C_6$ carbides in all alloys examined. This was due to the passage of the finer $Cr_{23}C_6$ carbides through the 0.1 μm filter paper. M_3B_2 boride peaks were evident in KM4 but were less distinct in the other alloys. SR3 also had evidence of small HfO_2 peaks. Most alloys had clear γ/γ′ peaks, indicating these phases were also present in the carbide extractions. René 88 DT and IN-100 carbide extractions had much smaller γ/γ′ peaks, indicating very little γ and γ′ contamination. Therefore, the chemistries of the carbide extractions listed in table 4 reflect the presence of the γ, γ′, borides and oxides extracted along with the carbides, but still provide useful information. The molybdenum and boron levels are higher than nominal for the alloys, and confirm the presence of $(Mo,Cr)_3B_2$ in all the alloys. The high titanium levels indicate titanium rich MC carbides. The high tantalum level in the CH98 carbide extraction reflect the presence of (Ta,Ti)C carbides.

Results of γ′ extractions are listed in tables 6 and 7. The γ′ extractions were filtered using the finest (0.1 μm) filter paper available. This was expected to capture the primary, secondary, and cooling γ′ particles, but not the finer aging γ′.

X-ray diffraction results of the γ′ extractions allowed calculation of the γ′ lattice parameters listed in table 6. In most cases the samples produced superlattice peaks. The lattice parameters represent the relaxed lattices and do not take into account changes in lattice parameters from stresses induced by mismatch between the γ and γ′. CH98 had the largest γ′ lattice parameter, and IN-100 the smallest. The table also lists the error limits for the lattice parameters. In all cases the lack of data from high angle diffraction peaks increased the errors. The CH98 which only had four observed peaks also suffered from increased uncertainty in the regression itself. The errors are somewhat larger than those typically quoted for lattice parameter results. It would have been advantageous to measure at least one higher angle peak to reduce the errors.

Chemical analyses of the γ′ and γ phases are listed in table 7. Also listed in table 7 are γ compositions calculated by mass balance (4) for each element. The calculated compositions are based on the nominal alloy composition, measured γ′ composition and weight fraction, and carbide composition and weight fraction. In general there was good agreement between the measured and calculated γ′ compositions.

Partitioning ratios indicate the tendency of an element to go into either the γ or γ′ phase. The partitioning ratios were calculated using the formula

$$P = \frac{\gamma_{at.\%}}{\gamma'_{at.\%}}$$ [1]

where $\gamma_{at.\%}$ and $\gamma'_{at.\%}$ are the atomic percentage of the element in the γ and γ' phase respectively. The results are listed in table 8.

René 88 DT and SR3 had notable differences as compared to the 18Co-12Cr alloys. These two alloys had lower cooling γ' weight fractions as determined by phase extraction than the other alloys; René 88 DT had the lowest at only 38.6 weight percent. This agrees with the TEM image analyses, and can be largely attributed to the lower Al and Ti contents of these alloys.

The differences in bulk chemistries of these alloys produced differences in phases compositions as well. It was observed in the γ phase that René 88 DT and SR 3 had the lowest Al and Co contents, and highest Ni content They also had the lowest Al and Co contents, and highest Ti content in the γ' phase. René 88 DT had the highest Cr content in the γ' phase. Among refractory elements, SR3 had the highest Mo content in the γ phase, while René 88 DT had the highest Mo and W content in the γ' phase. The other refractory elements (Nb, Hf, Ta) partitioned to the γ' phase, as previously observed (4,5). Ta in CH98 partitioned strongly to the γ', and had a higher concentration than Ti there. The Cr partitioning ratio varied substantially among the alloys, ranging from 5.8 for René 88 DT to 15.4 for 456-FC.

The determination of the lattice parameters and chemical compositions for the γ' also allows for the conversion of the area fraction determined in the image analysis to a weight fraction. The area fractions of γ' were converted into weight fractions by determining the average atomic weight of the atoms within the unit cell. For γ', the number of atoms per unit cell is equal to 4. The density of the γ' and γ phases were calculated using the equation

$$\rho = \frac{4\overline{w}}{a_o N}$$ [2]

where ρ is the density of the phase, $\overline{w}$ is the average atomic weight of the atoms in the unit cell based on the chemistry and atomic weights, a_o is the lattice parameter of the phase and N is Avagadro's number (6.023×10^{23}). To convert the area fraction of γ' ($A_{\gamma'}$) into a weight fraction ($W_{\gamma'}$), the equation

$$W_{\gamma'} = \frac{A_{\gamma'}\rho_{\gamma'}}{A_{\gamma'}\rho_{\gamma'} + A_{\gamma}\rho_{\gamma}}$$ [3]

was used. The results are presented in table 9. In the case of KM4 samples with grain sizes 3 and 9, extractions were not conducted. The assumption was made that the chemistries of the γ' and γ were the same for these samples as the KM4 sample with a grain size of ASTM 6. The agreement between the weight fractions calculated from image analysis and the extracted weight fractions were normally within 5 wt.%.

Comparison of Alloys

The microstructures of these alloys could be divided into two general classes based on chemistry and the solution/cooling heat treatments applied. Alloys given supersolvus solution and single step cooling heat treatments had similar ASTM 6-7 grain sizes, similar cooling and aging γ' sizes and morphologies, and generally similar distributions of $Cr_{23}C_6$ carbides predominantly at the grain boundaries. René 88 DT and SR3

had lower cooling γ′ contents than the 18Co-12Cr alloys due to chemistry differences. SR3 had the lowest carbide frequency at grain boundaries among these alloys. Extended supersolvus solutions of KM4 to produce a coarser ASTM 3 grain size produced a similar γ′ distribution but a higher density of $Cr_{23}C_6$ at the grain boundaries than the other alloys. This is consistent with the lower total grain boundary area of the coarsest grain material.

Subsolvus solution treatment of KM4 for ASTM 9 grain size produced a finer cooling γ′ size and very low density of $Cr_{23}C_6$ carbides. The finer cooling γ′ size may be associated with the low subsolvus quenching temperature, allowing less time for cooling γ′ to grow during quenching. The low carbide density is consistent with the high total grain boundary area of this fine grain material, and the associated dilution of elements that segregate to the grain boundaries to form carbides. The general characteristics of the microstructure, i.e., the morphology of γ′ present, were very similar to that produced by a supersolvus solution and single step cooling and aging heat treatment.

The other general class of microstructures was produced by serration cooling multistep supersolvus-subsolvus solution heat treatments. This produced a more complex γ′ phase distribution of coarse intragranular and intergranular secondary γ′, along with cooling and aging γ′. The secondary γ′ apparently formed during the supersolvus-subsolvus transition step of the heat treatment (see table 1). The cooling γ′, which subsequently formed after subsolvus solutioning, was finer than that of the ASTM 6 materials given single step cooling treatments. This also may be explained in part by the lower, subsolvus final solution temperature in the serration cool heat treatments..

Differences among the phase chemistries were apparent, associated with differences in nominal alloy chemistries. René 88 DT and SR3 had significantly different γ and γ′ compositions from the other alloys, with variations in Al, Co, and Ni levels. The associated elemental partitioning ratios varied with nominal alloy composition, with René 88 DT and SR3 again having the largest differences. However, the general trends agreed with previous work (2,3,4). Among refractory element additions, Nb, Ta, and Hf were found to be strong γ′ partitioners, Mo partitioned more to γ, while nearly equal partitioning of W between γ and γ′ seemed indicated.

Summary and Conclusions

The microstructures of the two general composition classes of powder metallurgy nickel-based superalloys were characterized by TEM and other methods. The γ′ content and phase compositions of the 18Co-12Cr alloys KM4, CH98, IN-100, and 456 had many similarities while René 88 DT and SR3 which had lower Al and Co and higher Cr contents than the 18Co-12Cr alloys produced lower γ′ content and different γ and γ′ phase compositions. However, KM4, CH98, SR3, René 88 DT, and Alloy 456 had generally similar microstructures when given fast cool single step supersolvus solution treatments to produce a grain size near ASTM 6. Their resulting γ′ size distributions, grain boundary serrations, and grain boundary carbide frequencies and densities were generally similar. When the solution temperature and time for KM4 were modified to produce coarser ASTM 3 and finer ASTM 9 grain sizes, the density of grain boundary carbides was substantially increased for ASTM 3 and decreased for ASTM 9. IN-100 and Alloy 456 subjected to multistep serration cool heat treatments had more complex γ′ phase distributions consisting of coarse intragranular and intergranular secondary γ′ and finer than average cooling γ′, and aging γ′. The density of grain boundary carbides in IN-100 was similar to the fast cool ASTM 6 alloys, however Alloy 456-SC had a variable density of grain boundary carbides.

It can be concluded from this evaluation that

(1) In spite of the composition differences among these alloys, similar supersolvus solution and single step cooling heat treatments can produce quite similar microstructures.

(2) $Cr_{23}C_6$ carbides predominate along the grain boundaries of these disk alloys. The density of these carbides at grain boundaries can be a strong function of the grain size.

(3) Multi-step serration cool solution treatments significantly alter the γ' phase distribution.

(4) Stabilization heat treatments employed in this study result in coarsened final aging γ' size but does not improve carbide uniformity.

(5) The chemistries of the phases were significantly different among the alloys, and elemental partitioning ratios varied with alloy composition.

References

1. D.F. Paulonis, HSR–EPM Coordination Memo 05–P93060808, June 8, 1993.

2. HSR–EPM Coordination Memo 05–93072811, July 29, 1993.

3. H.L. Danflou, M. Marty, and A. Walder, "Formation of Serrated Grain Boundaries and Their Effect on the Mechanical Properties in a P/M Nickel Base Superalloy", Superalloys 1992, ed. S.D. Antolovich, et al., The Metallurgical Society of AIME, Warrendale, PA, 1992, pp. 63–72.

4. O.H. Kriege and J.M. Baris, "The Chemical Partitioning of Elements in Gamma Prime Separated From Precipitation-Hardened, High-Temperature Nickel-Base Alloys", Transactions of the ASM, vol. 62, 1969, pp. 195–200.

5. Y.C. Fayman, "Microstructural Characterization and Elemental Partitioning in a Direct-aged Superalloy (DA 718), Materials Science and Engineering, vol. 92, 1987, pp. 159–171.

6. H.E. Collins, "Relative Long-Time Stability of Carbide and Intermetallic Phases in Nickel-Base Superalloys", Transactions of the ASM, vol. 62, 1969, pp. 82–104.

TABLE 1.—NOMINAL COMPOSITIONS, GRAIN SIZES AND HEAT TREATMENTS OF BASELINE ALLOYS

	Alloy								
	456-FC	456-SC	CH98	IN-100	KM4			René 88 DT	SR3
ASTM Grain size	6	6	6	6	3	6	9	6	6
Heat treatment	1205 °C/2h + AC + 815 °C/4h + 735 °C/8h	1200 °C/2h + cool 4 °C/min to 1120 °C + AC + 815 °C/4h+ 735 °C/8h	1135 °C/1h + 1220 °C/2h + AC + 775°C/8h	Proprietary	1190 °C/3h + AC + 775 °C/8h	1185 °C/3h + AC + 775 °C/8h	1165 °C/3h + AC + 775 °C/8h	1150 °C/1h + OQ + 760 °C/8h	1135 °C/1h + 1190 °C/3h + AC + 775 °C/8h
Al	4.6	4.6	4.0	5	4.0	4.0	4.0	2.1	2.6
B	0.03	0.03	0.03	0.02	0.03	0.03	0.03	0.015	0.015
C	0.05	0.05	0.03	0.07	0.03	0.03	0.03	0.05	0.03
Co	18.6	18.6	18.0	18.5	18.0	18.0	18.0	13.0	11.9
Cr	12.5	12.5	12.0	12.4	12.0	12.0	12.0	16.0	12.8
Hf									0.2
Mo	3.3	3.3	4.0	3.2	4.0	4.0	4.0	4.0	5.1
Nb	1.0	1.0			2.0	2.0	2.0	0.7	1.6
Ni	Bal.	Bal.	Bal.	Bal.	Bal.	Bal.	Bal.	Bal.	Bal.
Ta			3.8						
Ti	3.9	3.9	4.0	4.3	4.0	4.0	4.0	3.7	4.9
V				0.80					
W	3.2	3.2						4.0	
Zr	0.06	0.06	0.03	0.06	0.03	0.03	0.03	0.05	0.03

All compositions in weight percent.

TABLE 2(a).—COOLING γ′ PRECIPITATE SIZES

		456 FC	456 SC	CH98	IN-100 CG	KM4 - ASTM 3	KM4 - ASTM 6	KM4 - ASTM 9	René 88 DT	SR3
Number		548	107	70	66	38	38	51	123	144
Area fraction		61.2%	61.7%	59.5%	56.2%	47.5%	52.9%	56.0%	35.6%	44.0%
Weight fraction		60.0%	60.3%	59.4%	54.8%	46.2%	51.6%	54.7%	35.0%	42.5%
Major axis	Average	212.80	140.28	236.19	242.73	242.68	393.80	204.99	234.11	312.39
	σ	55.76	43.26	107.50	97.39	72.97	127.24	6.09	92.08	146.12
	Minimum	43.51	37.57	95.12	89.30	70.51	130.58	69.97	70.46	80.33
	Maximum	470.93	354.46	582.06	545.53	357.96	758.90	345.91	543.28	634.09
Minor axis	Average	147.77	110.36	172.34	161.53	183.40	318.59	146.61	179.45	233.44
	σ	52.89	35.38	84.53	78.47	71.27	114.28	59.70	78.29	126.12
	Minimum	0.00	30.29	56.38	51.52	43.04	95.48	44.76	33.47	37.87
	Maximum	309.61	223.63	512.91	384.05	307.00	597.86	292.13	395.70	498.26
Feret Diameter	Average	164.88	118.15	191.33	185.21	199.34	317.36	164.53	187.90	243.77
	σ	37.85	31.49	81.37	72.10	62.38	90.48	55.57	71.44	107.28
	Minimum	42.52	35.79	74.22	68.94	55.41	111.40	54.81	55.11	56.94
	Maximum	279.92	250.55	484.23	417.63	296.88	535.94	269.65	371.81	471.59
Aspect ratio	Average	0.69	0.79	0.74	0.66	0.74	0.81	0.71	0.76	0.73
	σ	0.17	0.13	0.16	0.14	0.13	0.12	0.13	0.12	0.13
	Minimum	0.00	0.38	0.33	0.30	0.48	0.45	0.44	0.34	0.41
	Maximum	1.00	1.00	0.98	0.97	0.98	0.98	0.91	0.97	0.98
Compactness	Average	27.53	16.55	17.02	21.34	16.01	19.29	16.63	28.84	21.35
	σ	11.45	3.71	3.15	11.90	1.09	4.98	1.39	17.31	8.08
	Minimum	10.89	12.76	13.96	14.06	14.22	14.39	14.30	14.31	13.66
	Maximum	123.17	45.08	30.20	94.10	18.15	32.75	20.63	97.76	67.59
Shape factor	Average	0.52	0.76	0.76	0.66	0.79	0.69	0.76	0.54	0.65
	σ	0.16	0.01	0.11	0.16	0.05	.14	0.06	0.20	0.18
	Minimum	0.10	0.28	0.42	0.13	0.69	0.38	0.61	0.13	0.19
	Maximum	1.15	0.98	0.90	0.89	0.88	0.87	0.88	0.88	0.92

All sizes in nanometers.
Shape factors greater than 1 caused by precipitates with a very small (typically <15) number of pixels.

TABLE 2(b).—AGING γ´ PRECIPITATE SIZES

		456 FC	456 SC	CH98	IN-100 CG	KM4 - ASTM 3	KM4 - ASTM 6	KM4 - ASTM 9	René 88 DT	SR3
Number		51	64	51	404	53	77	65	112	283
Major axis	Average	48.52	69.96	44.74	18.04	15.26	41.52	22.85	22.52	26.00
	σ	16.36	31.91	21.27	12.36	4.85	17.42	8.02	12.08	12.39
	Minimum	17.43	30.37	8.97	1.54	5.15	9.81	7.00	5.37	2.50
	Maximum	86.93	181.03	134.73	90.23	34.36	83.75	40.42	84.33	85.15
Minor axis	Average	34.49	50.63	30.64	13.44	11.92	33.00	16.64	17.32	18.12
	σ	9.80	23.00	19.00	9.60	3.84	15.16	6.44	9.34	9.59
	Minimum	14.48	15.06	5.56	0.00	5.15	8.34	4.34	4.24	0.00
	Maximum	57.61	136.39	84.21	65.83	27.78	69.91	33.98	56.41	52.43
Feret Diameter	Average	40.96	57.90	37.60	16.34	14.76	36.99	19.82	19.83	23.58
	σ	10.52	23.68	21.92	10.35	4.07	15.39	6.36	9.55	9.64
	Minimum	18.27	18.51	10.12	2.46	5.82	9.76	6.58	5.66	3.99
	Maximum	63.18	143.53	107.56	76.15	31.35	72.46	36.29	60.47	63.21
Aspect ratio	Average	0.74	0.74	0.70	0.75	0.80	0.77	0.73	0.78	0.72
	σ	0.14	0.14	0.16	0.16	0.13	0.12	0.15	0.13	0.22
	Minimum	0.39	0.35	0.38	0.00	0.44	0.43	0.38	0.43	0.00
	Maximum	0.95	0.94	0.93	1.00	1.00	0.96	0.96	1.00	1.00
Compactness	Average	15.63	15.30	15.36	13.91	13.35	14.71	14.74	16.37	15.26
	σ	3.45	1.80	1.90	1.89	1.07	1.13	1.59	3.90	4.25
	Minimum	12.33	12.68	10.89	8.00	11.49	12.90	12.23	11.99	8.00
	Maximum	34.51	25.85	20.52	22.01	15.68	19.41	19.41	34.69	39.46
Shape factor	Average	0.83	0.83	0.83	0.92	0.95	0.85	0.86	0.80	0.87
	σ	0.12	0.08	0.61	0.12	0.08	0.07	0.09	0.14	0.19
	Minimum	0.36	0.49	.061	0.57	0.80	0.65	0.65	0.36	0.32
	Maximum	1.12	0.99	1.15	1.57	1.09	0.97	1.03	1.05	1.57

All sizes in nanometers.
Shape factors greater than 1 caused by precipitates with a very small (typically <15) number of pixels.

TABLE 2(c).—SECONDARY γ' PRECIPITATE SIZES

		456 SC - Intragranular	456 SC - Grain boundaries	IN-100 - Intragranular	IN-100 - Grain boundaries
Number		67	54	192	102
Major Axis	**Average**	1287.96	4424.62	1090.73	3047.97
	σ	547.8	3607.82	298.1	1103.94
	Minimum	438.6	1404.19	366.42	969.24
	Maximum	2649.27	17932.64	2249.13	5798.83
Minor Axis	**Average**	763.96	1660.91	910.21	2085.63
	σ	332.2	840.56	216.09	695.32
	Minimum	334.03	323.39	346.60	590.03
	Maximum	1799.85	5056.74	1613.78	3997.13
Feret Diameter	**Average**	827.46	2005.09	813.74	1747.52
	σ	311.33	875.78	214.38	695.54
	Minimum	376.91	743.04	248.38	197.64
	Maximum	1559.53	5625.09	1364.21	3618.73
Aspect Ratio	**Average**	0.62	0.44	0.76	0.59
	σ	0.16	0.18	0.13	0.18
	Minimum	0.36	0.09	0.35	0.15
	Maximum	0.99	0.89	1.00	0.99
Compactness	**Average**	79.52	218.25	19.27	42.39
	σ	44.4	258.68	5.56	84.45
	Minimum	17.42	36.93	12.87	13.8
	Maximum	202.28	1592.64	48.08	714.83
Shape Factor	**Average**	0.22	0.11	0.69	0.53
	σ	0.14	0.08	0.14	0.20
	Minimum	0.06	0.00	0.26	0.02
	Maximum	0.71	0.34	0.98	0.91

All sizes in nanometers.

TABLE 3(a).—CARBIDE, BORIDE AND OXIDE PARTICLE SIZE RANGES AND RELATIVE FREQUENCIES—INTRAGRANULAR

		456 FC	456 SC	CH98	IN-100 CG	KM4 - ASTM 3	KM4 - ASTM 6	KM4 - ASTM 9	René 88 DT	SR3
$Cr_{23}C_6$	**Percent**	ND	ND	ND	ND	ND	ND	ND	ND	ND
	Minimum									
	Maximum									
$(Ti,Nb)C$	**Percent**	100%	100%	100% (Ti,Ta)C	100% TiC	95%	85%	85%	95%	100%
	Minimum	100	200	150	200	200	150	150	100	200
	Maximum	500	400	500	600	700	600	600	250	600
$(Mo,Cr)_3B_2$	**Percent**	ND	ND	ND	ND	5%	15%	15%	5%	ND
	Minimum					500	500	500	900	
	Maximum					1,000	1,000	1,000	1,100	
Al_2O_3	**Percent**	Present	ND	Present	ND	Present	Present	Present	Present	ND
	Minimum	30		150		20	20	20	20	
	Maximum	150		500		100	80	70	100	
ZrO_2	**Percent**	Present	Present	Present	ND	Present	Present	Present	Present	ND
	Minimum	50	60	50		20	20	20	20	
	Maximum	250	225	100		100	80	70	100	
$(Hf,Zr)O_2$	**Percent**									Present
	Minimum									50
	Maximum									400

All sizes in nanometers.
ND = Not Detected
Present = Observed in small numbers (<5% of the total particles)

TABLE 3(b).—CARBIDE, BORIDE AND OXIDE PARTICLE SIZE RANGES AND RELATIVE FREQUENCIES—GRAIN BOUNDARIES

		456 FC	456 SC	CH98	IN-100 CG	KM4 - ASTM 3	KM4 - ASTM 6	KM4 - ASTM 9†	René 88 DT	SR3
$Cr_{23}C_6$	Percent	90%	90%	90%	95%	90%	90%	ND	90%	95%
	Minimum	20	20	20	20	20	20		20	10
	Maximum	110	100	120	90	120	100		80	100
$(Ti,Nb)C$	Percent	5%	5%	5% (Ti,Ta)C	5% TiC	5%	5%	Very sparse	5%	5%
	Minimum	150	200	350	200	400	150		270	300
	Maximum	500	500	1,000	600	600	600		330	600
$(Mo,Cr)_3B_2$	Percent	5%*	5%*	5%	ND	5%	5%	ND	5%*	ND
	Minimum	500	1,000	1,000		1,300	500		900	
	Maximum	>3,200	>4,600	>1,600		1,900	1,000		1,100	
Al_2O_3	Percent	ND	ND	Present	ND	ND	ND	Very sparse	ND	ND
	Minimum			100						
	Maximum			400						
ZrO_2	Percent	ND	ND	ND	ND	ND	ND	ND	ND	ND
	Minimum									
	Maximum									
$(Hf,Zr)O_2$	Percent									Present
	Minimum									300
	Maximum									600

*$(Mo,Cr,W)_3B_2$
All sizes in nanometers.
ND = Not Detected
Present = Observed in small numbers (<5% of the total particles)
†98% of viewed grain boundaries had no detectable grain boundary phases.

TABLE 4.—X-RAY ANALYSIS OF CARBIDE EXTRACTIONS

Alloy	Phase 1		Phase 2		
	Type	a_o, nm	Type	a_o, nm	c_o, nm
456-SC	MC	0.437			
CH98	MC	0.438			
IN-100	MC	0.431			
KM4 ASTM 6	MC	0.438	M_3B_2	0.580	0.310
René 88 DT	MC	0.435	M_3B_2	0.580	0.312
SR3 ASTM 6	MC	0.438			

TABLE 5.—WEIGHT PERCENT AND CHEMICAL COMPOSITION OF CARBIDES EXTRACTIONS

Element	Alloy					
	456-SC	CH98	IN-100	KM4 ASTM 6	René 88 DT	SR3 ASTM 6
Weight percent	0.96	0.25	0.11	0.17	0.21	1.25
Al	4.20	3.80	1.70	4.10	0.90	2.80
B	0.20	0.30	0.80	1.00	0.90	0.01
Co	16.80	12.00	1.10	13.50	0.60	11.50
Cr	13.30	9.70	7.10	12.20	4.00	13.00
Hf						1.40
Mo	4.80	4.70	21.00	12.00	6.40	5.50
Nb	3.60			8.80	14.80	2.00
Ni	43.70	35.70	2.10	38.80	2.60	58.20
Ta		22.60				
Ti	7.20	10.80	63.00	9.00	23.40	5.40
V			2.40			
W	3.60				40.90	
Zr	1.00	0.30	0.90	0.60	5.40	0.10

All compositions in weight percent.

TABLE 6.—LATTICE PARAMETERS OF EXTRACTED γ'

Alloy	Peaks measured	Lattice parameter, Å	95 percent confidence limit, Å
456-FC	6	3.595	± 0.006
456-SC	6	3.573	± 0.022
CH98	4	3.632	± 0.210
IN-100	8	3.585	± 0.003
KM4 ASTM 6	6	3.598	± 0.007
René 88 DT	6	3.587	± 0.013
SR3 ASTM 6	6	3.599	± 0.007

TABLE 7(a).—WEIGHT FRACTIONS AND CHEMICAL COMPOSITIONS OF γ AND γ´

	Alloy													
	456-FC		456-SC		CH98		IN-100		KM4 ASTM 6		René 88 DT		SR3	
Element	γ	γ´	γ	γ´	γ	γ´	γ	γ´	γ	γ´	γ	γ´	γ	γ´
Weight percent	41.5	58.5	42.3	56.7	42.2	57.8	40.2	59.7	43.8	56.0	61.2	38.6	51.7	47.1
Ni:Al	11.1	3.0	9.0	2.9	10.6	3.2	8.1	2.8	12.1	3.0	18.5	3.1	22.5	3.1
Al	1.40	6.60	1.50	6.90	1.40	5.60	2.00	7.10	1.30	6.40	0.90	4.60	0.70	5.10
B	0.100	0.000	0.062	0.000	0.050	0.000	0.060	0.000	0.073	0.000	0.000	0.000	0.044	0.000
Co	28.90	8.70	29.10	10.30	27.60	7.70	28.20	11.40	27.80	9.60	16.80	4.50	17.10	5.40
Cr	21.70	1.50	25.40	2.40	19.80	1.50	24.30	3.40	22.90	2.90	21.50	3.80	21.30	2.50
Hf													0.0	0.3
Mo	3.80	1.50	5.60	1.60	4.70	1.50	5.20	1.60	6.70	1.80	4.80	2.60	8.30	1.40
Nb	0.20	1.60	0.20	1.70					0.40	3.40	0.20	1.80	0.60	2.90
Ni	33.20	65.30	33.80	67.80	37.40	63.20	39.20	68.60	40.30	68.60	52.20	67.60	50.80	72.40
Ta					0.00	6.70								
Ti	0.50	6.10	0.40	6.50	0.40	6.30	0.40	7.20	0.40	7.10	0.70	9.80	0.60	10.00
V							0.60	0.50						
W	2.80	2.20	4.00	3.10							2.80	5.40		
Zr	0.000	0.000	0.000	0.056	0.000	0.080	0.000	0.028	0.000	0.000	0.000	0.100	0.000	0.000
Ni+Co	62.10	74.00	62.90	78.10	65.00	70.90	67.40	80.00	68.10	78.20	69.00	72.10	67.90	77.80

All compositions in weight percent.

TABLE 7(b).—COMPARISON OF CALCULATED AND MEASURED γ CHEMISTRIES (wt.%)

Element	456-SC Calculated	456-SC Measured	CH98 Calculated	CH98 Measured	IN-100 Calculated	IN-100 Measured	KM4 ASTM 6 Calculated	KM4 ASTM 6 Measured	René 88 DT Calculated	René 88 DT Measured	SR3 Calculated	SR3 Measured
Al	1.54	1.40	1.62	1.40	1.89	2.00	0.90	1.30	0.52	0.90	0.31	0.70
B	.066	0.10	0.060	0.050	0.050	0.060	0.060	0.073	0.020	0.000	0.029	0.044
Co	29.90	28.90	29.30	27.60	29.02	28.20	28.70	27.80	18.40	16.80	17.84	17.10
Cr	26.12	21.70	24.04	19.80	25.72	24.30	23.58	22.90	23.73	21.50	22.20	21.30
Hf											0.077	0.00
Mo	5.58	3.80	6.75	4.70	5.51	5.20	6.76	6.70	4.87	4.80	8.47	8.30
Nb	0.07	0.20					0.18	0.40	0.00	0.20	0.41	0.60
Ni	32.98	33.20	37.42	37.40	36.47	39.20	39.69	40.30	49.48	52.20	50.37	50.80
Ta			0.15	0.00								
Ti	0.36	0.50	0.71	0.40	0.00	0.40	0.02	0.40	0.00	0.70	0.23	0.60
V					1.24	0.60						
W	3.35	2.80							2.99	2.80		
Zr	0.045	0.000	0.000	0.000	0.100	0.000	0.070	0.000	0.000	0.000	0.056	0.000

Mass balance calculated using nominal alloy composition and measured γ′ composition.
All compositions in weight percent.

TABLE 8.—PARTITIONING RATIOS

Element	Alloy						
	456-FC	456-SC	CH98	IN-100	KM4 ASTM 6	René 88 DT	SR3 ASTM 6
Al	0.23	0.23	0.25	0.30	0.21	0.2	0.15
B	-----	-----	-----	-----	-----	-----	-----
Co	3.54	2.99	3.65	2.61	3.05	3.8	3.38
Cr	15.40	11.21	13.44	7.55	8.31	5.8	9.09
Hf							0.00
Mo	2.70	3.71	3.19	3.43	3.92	1.9	6.32
Nb	0.13	0.13			0.12	0.1	0.22
Ni	0.54	0.53	0.60	0.60	0.62	0.8	0.75
Ta			0.00				
Ti	0.09	0.07	0.07	0.06	0.06	0.1	0.06
V				1.27			
W	1.36	1.37				0.5	
Zr	-----	0.00	0.00	0.00	-----	0.0	-----

TABLE 9.— γ' AREA AND WEIGHT FRACTIONS

Alloy	Image analysis		Chemical analysis
	Area fraction	Weight fraction	Extracted weight fraction
456-FC	61.2%	60.0%	58.5%
456-SC	61.7%	60.3%	56.7%
CH98	59.5%	59.4%	57.8%
IN-100	56.2%	54.8%	59.7%
KM4 ASTM 3*	47.5%	46.2%	N/A
KM4 ASTM 6	52.9%	51.6%	56.0%
KM4 ASTM 9*	56.0%	54.7%	N/A
Rene 88 DT	35.6%	35.0%	38.6%
SR 3	44.0%	42.5%	47.1%

*Image analysis—weight fraction based on KM 4 ASTM 6 chemistries.

Appendix A
Determination of Weight Fraction of γ´ from Chemical Analyses

Extractions were used to experimentally determine the weight fraction of γ´ in each alloy. However, a check is available to determine the weight fraction of γ´ from the chemical analyses of the bulk alloy, γ and γ´. The method also has the ability to highlight questionable chemical analyses.

Consider a two element phase diagram such as that presented in figure A–1. From the phase diagram the concentration of A and B in α (C_α^A and C_α^B) and β (C_β^A and C_β^B) can be determined at any temperature T. The concentration of A and B in the alloy (C_{Alloy}^A and C_{Alloy}^B) are also known. The reverse lever rule can be used to determine the weight fraction of β, f_β, present. This yields two equations,

$$f_\beta = \frac{C_{Alloy}^A - C_\alpha^A}{C_\alpha^A - C_\beta^A} \quad\quad\quad\quad \text{[A–1]}$$

$$f_\beta = \frac{C_{Alloy}^B - C_\alpha^B}{C_\alpha^B - C_\beta^B} \quad\quad\quad\quad \text{[A–2]}$$

The equations can be rearranged to the following

$$f_\beta(C_\alpha^A - C_\beta^A) = (C_{Alloy}^A - C_\alpha^A) \quad\quad\quad\quad \text{[A–3]}$$

$$f_\beta(C_\alpha^B - C_\beta^B) = (C_{Alloy}^B - C_\alpha^B) \quad\quad\quad\quad \text{[A–4]}$$

In this form it is obvious that the equations describe a straight line with X axis being $C_\alpha^x - C_\beta^x$ and the Y axis being $C_{Alloy}^x - C_\alpha^x$. Here *x* is either element A or B depending on which equation is used. It is desirable to have the X and Y axes the same for both equations. For a two element alloy,

$$C_x^B = 1 - C_x^A \quad\quad\quad\quad \text{[A–5]}$$

Substituting equation [A–5] into equation [A–4] yields equation [A–3]. Therefore a plot such as the one in figure A–2 can be constructed without the need to normalize all results to one element's concentration. For the ideal case the slope of the curve is equal to the weight fraction of the phase of interest (β) and the intercept is equal to 0. Deviations from the ideal case are an indication of how inaccurate the measurements of the various concentrations are.

For a more complex, *n*-element alloy, the same concepts apply. In the narrowly defined case of the alloy having only two phases, equations [A–3] and [A–4] can be extended to the generalized form of

$$f_\beta(C_\alpha^x - C_\beta^x) = C_{Alloy}^x - C_\alpha^x \quad\quad\quad\quad \text{[A–6]}$$

and a plot with the same axes again generates an ideal line with a slope equal to the weight fraction of the β phase and an intercept of 0.

In the case of an *n*-element alloy, the plot can also yield additional information. The line for the plot is generated through a least squares regression analysis. Deviations between the predicted and observed values should be small if the analysis of the alloy is performed properly. However, if one element is analyzed or reported incorrectly, the difference between the predicted and observed values will be larger. The regression analysis will also yield indications that the goodness of fit for the line is poor. Therefore the plot can be used to also assess the quality of the chemical analyses as well as the extractions.

Based on this analysis the weight fractions of γ′ for each alloy were determined by plotting the chemical analyses as in figure A–2. An example is shown in figure A–3 for the 456-FC chemical analysis. The best fit line was determined using least squares regression. The fit of the curves was excellent ($r^2 > 0.99$) with no gross deviations from the regression line observed for any of the data points. The results of the plotting and linear regression analysis are shown in table A–1 along with the results reported in table 9 from image analysis and phase extraction work. The values are in good agreement for all alloys except René 88 DT. In the case of René 88 DT the image analysis and extracted weight fractions agreed with the expected results, but the weight fraction calculated by this method was significantly lower. There was no good explanation for the discrepancy.
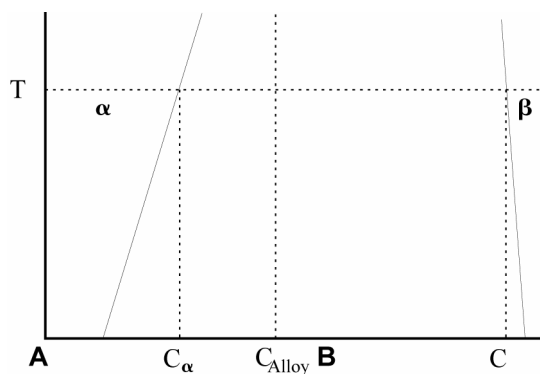
Figure A–1.—Typical two element phase diagram.
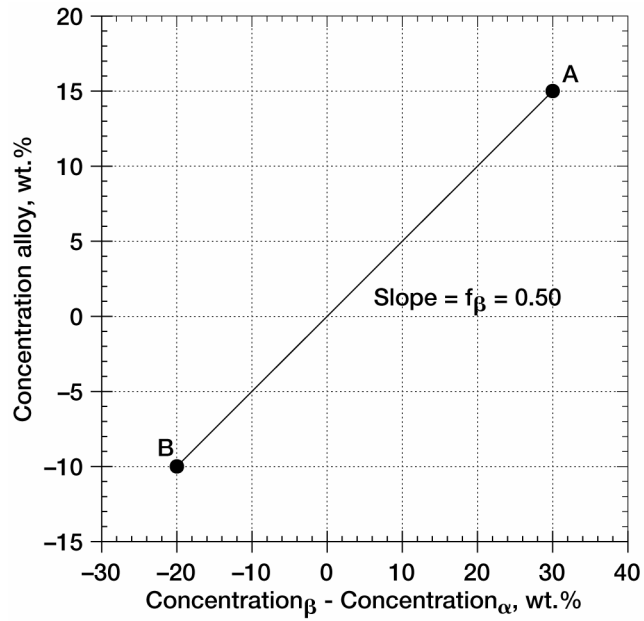
Figure A–2.—Plot of C_{alloy}^x versus $C_\alpha^x - C_\beta^x$ for two elements.
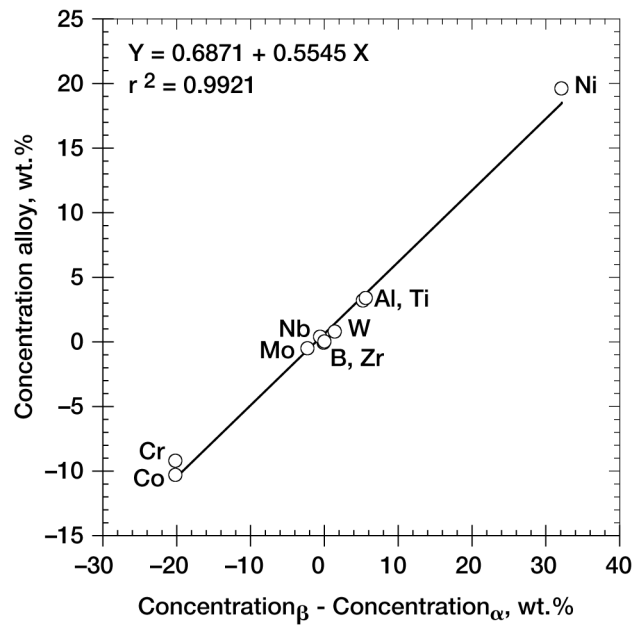
Figure A-3.—Plot for 456-FC.

TABLE A–2.—γ´ WEIGHT FRACTIONS AND AREA FRACTIONS

Alloy	Image analysis		Chemical analysis	
	Area fraction	Weight fraction	Extracted weight fraction	Calculated weight fraction
456-FC	61.2%	60.0%	58.5%	55.5%
456-SC	61.7%	60.3%	56.7%	56.0%
CH98	59.5%	59.4%	57.8%	54.5%
IN-100	56.2%	54.8%	59.7%	56.6%
KM4 ASTM 3*	47.5%	46.2%	N/A	N/A
KM4 ASTM 6	52.9%	51.6%	56.0%	54.7%
KM4 ASTM 9*	56.0%	54.7%	N/A	N/A
Rene 88 DT	35.6%	35.0%	38.6%	30.3%
SR 3	44.0%	42.5%	47.1%	45.7%

*Image analysis—weight fraction based on KM4 ASTM 6 chemistries.

Appendix B
Mathematical Meanings of Various Image Analysis Numbers

Several terms and numbers are used to describe the shape and size of the precipitates. The sizes of the precipitates are described by the major and minor axes and the feret diameter. Figure B–1 shows the major and minor axes for a variety of different shapes. In all cases the major axis is defined as the longest chord that can be drawn between two points on the perimeter of the precipitate. After determining the major axis, the minor axis is defined as the longest chord perpendicular to the major axis. It should be noted that the major and minor axes are not constrained to fall entirely within the precipitate. If, for example, the precipitate is curved, the major axis can lie partially or completely outside the precipitate.
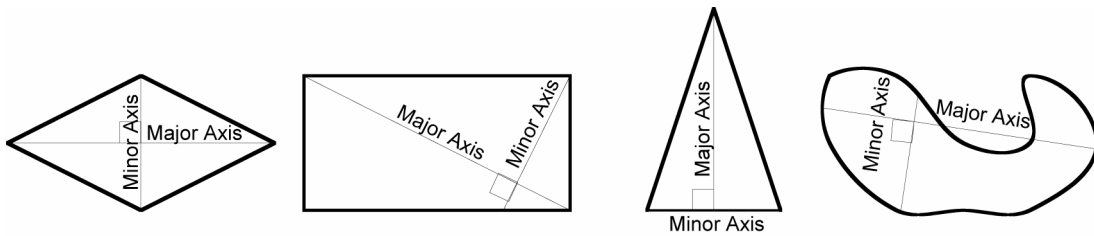
Figure B-1.—Major and minor axes for various shapes.

The feret diameter is defined in equation [B–1]. The feret diameter is useful in comparing the sizes of differently shaped precipitates because the sizes are normalized to be equal to circular precipitates with the same area. It is thus possible to readily compare the size of irregular precipitates to circular or square precipitates. In this paper the size distributions were all reported using the feret diameter of the precipitates.

$$\text{Feret Diameter} = \sqrt{\frac{4\text{Area}}{\pi}} \qquad [\text{B--1}]$$

Three numbers were used to quantitatively describe and compare the shapes of the precipitates. The most commonly used of the three is the aspect ratio. As shown in equation [B–2], the aspect ratio is the ratio of the length of the minor axis to length of the major axis. For a circle, a square and some other regular polyhedrons, the aspect ratio is 1. As the aspect ratio approaches 0, the precipitate lengthens. In the extreme case, a line has an aspect ratio of 0.

$$\text{Aspect Ratio} = \frac{\text{Minor Axis Length}}{\text{Major Axis Length}} \qquad [\text{B--2}]$$

The shape factor is a more general measure of the shape of a precipitate. The mathematical expression for the shape factor is presented in equation [B–3]. In the case of a circle, the shape factor is 1. However, the shape factor also has unique values for other regular polygons. The value of the shape factor is 0.86 for a pentagon, 0.79 for a square and 0.61 for an equilateral triangle. By comparing the shape factor to these idealized values, an approximation of the shape is possible.

$$\text{Shape Factor} = \frac{4\pi\text{Area}}{\text{Perimeter}^2} \qquad\qquad \text{[B--3]}$$

The third value used to describe the shape of the precipitates is compactness. As defined in equation [B–4], the compactness measures the ratio of the perimeter squared to the area. The compactness has a minimum value of 4π for a circle and tends to infinity as the shape of the particle tends to a line. Comparison of the compactness to the value for a circle measures the deviation of the precipitates from spherical.

$$\text{Compactness} = \frac{\text{Perimeter}^2}{\text{Area}} \qquad\qquad \text{[B--4]}$$

By utilizing the various measurements of the γ' size and shape generated through image analysis, the size and shape population distributions of the γ' precipitates as well as the average values can be understood and quantified. In turn, this information can be used in modeling studies to predict the behavior of the alloys.
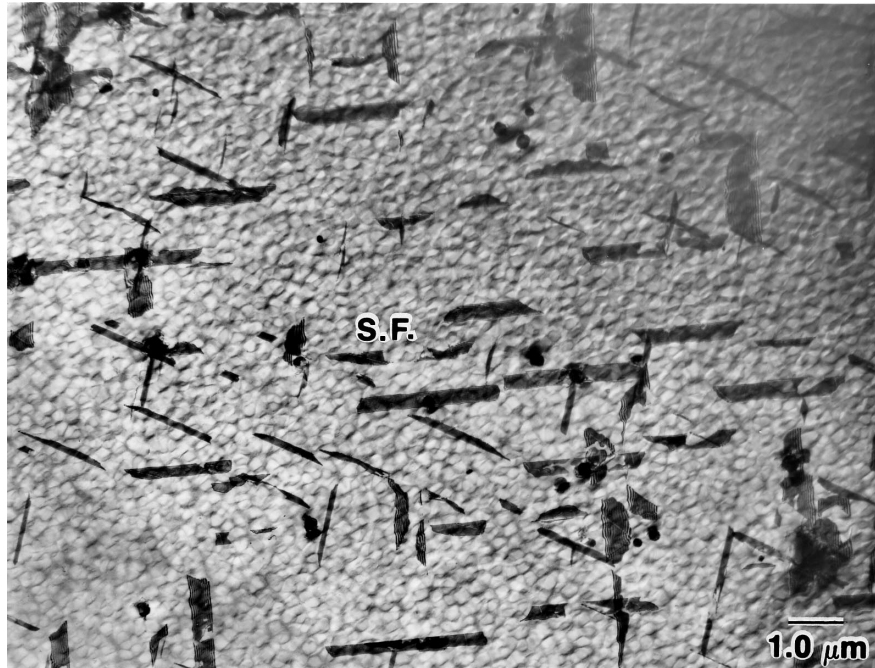
Figure 1(a).—Typical TEM micrograph showing general microstructure of KM4 ASTM 3, (S.F = stacking fault).
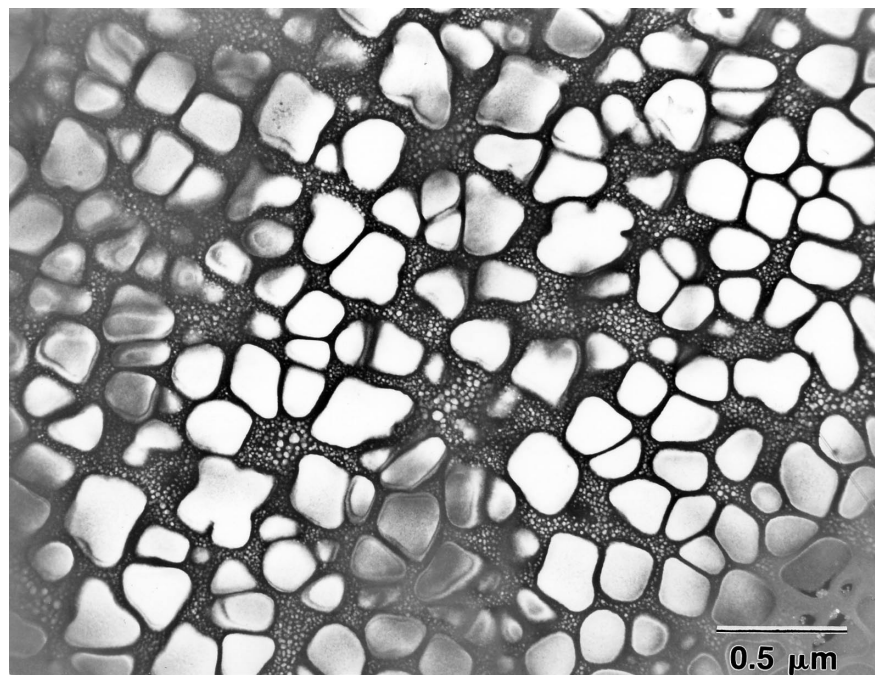
Figure 1(b).—Typical TEM micrograph showing γ' distribution of KM4 ASTM 3.
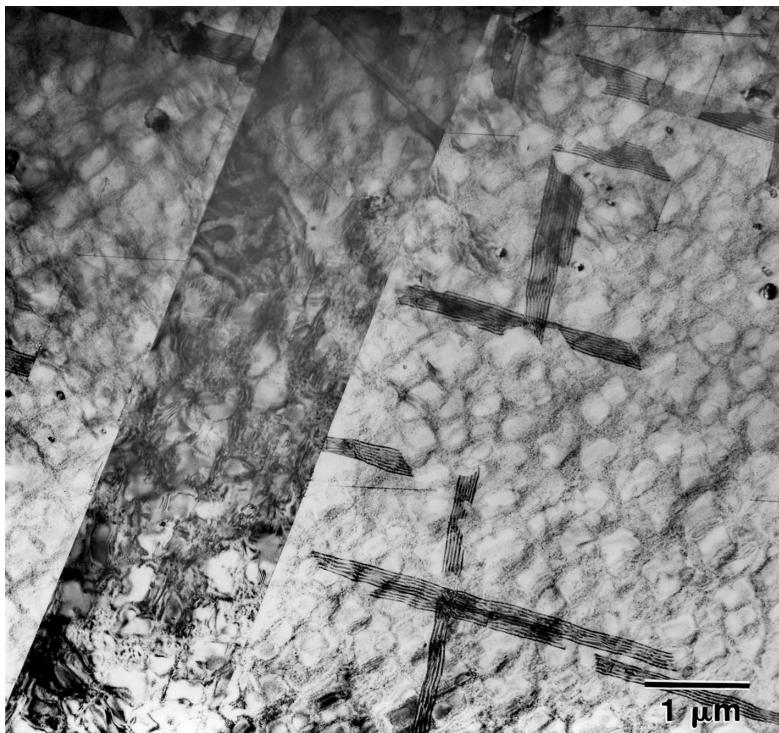
Figure 1(c).—Typical TEM micrograph showing general microstructure of KM4 ASTM 6.
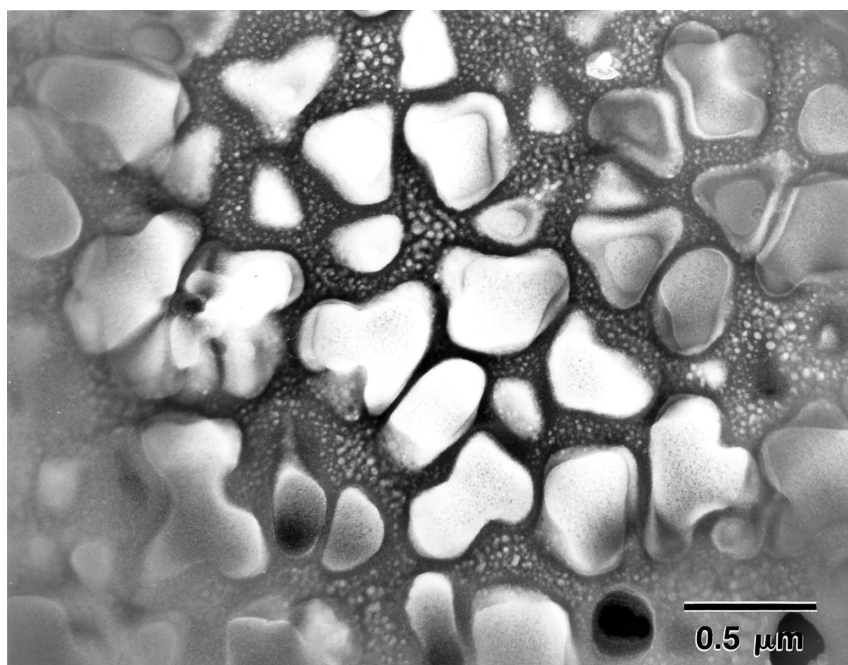
Figure 1(d).—Typical TEM micrograph showing γ' distribution of KM4 ASTM 6.

NASA/TM—2004-213123   28
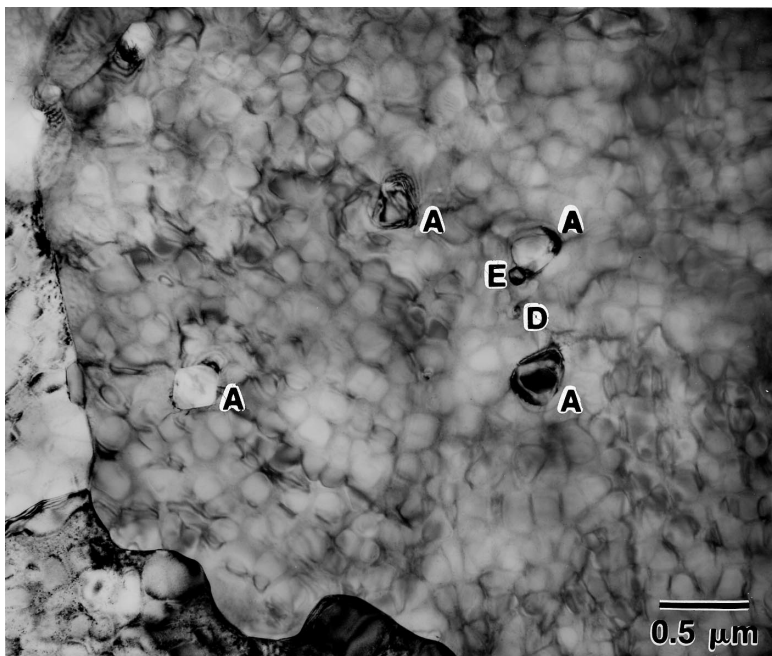
Figure 1(e).—Typical TEM micrograph showing general microstructure of KM4 ASTM 9 (A = (Ti,Nb)C, D = Al_2O_3, E = ZrO_2).
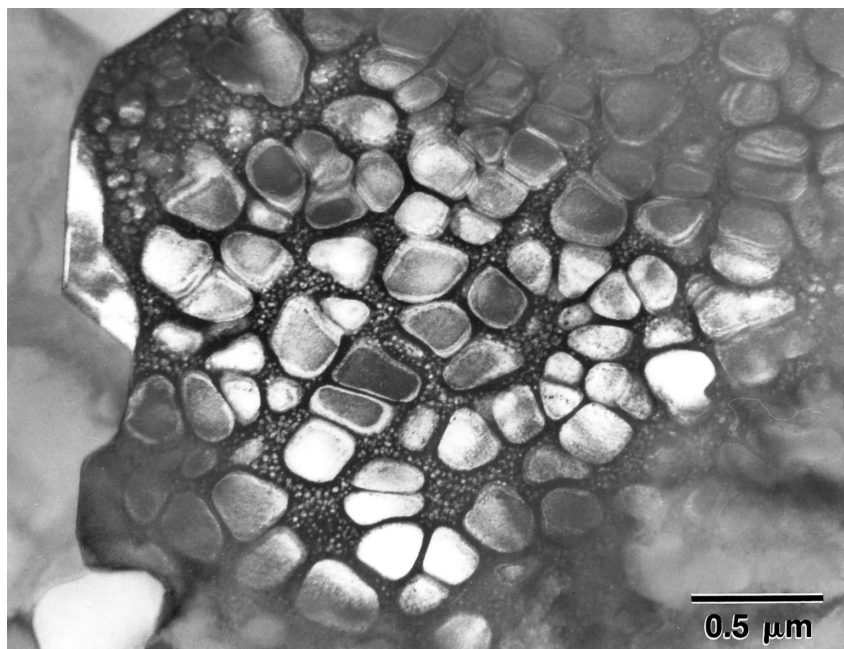
Figure 1(f).—Typical TEM micrograph showing γ' distribution of KM4 ASTM 9.
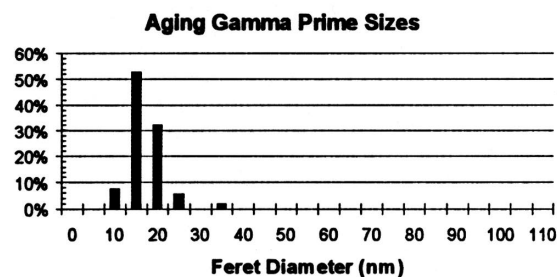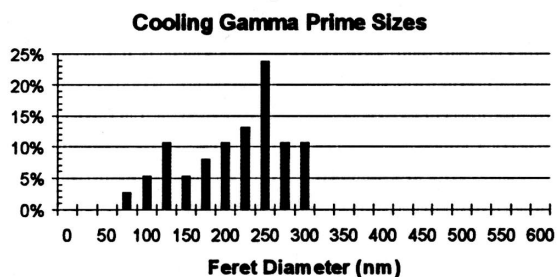
Figure 2(a).—γ' Feret diameter size distributions of KM4 ASTM 3.
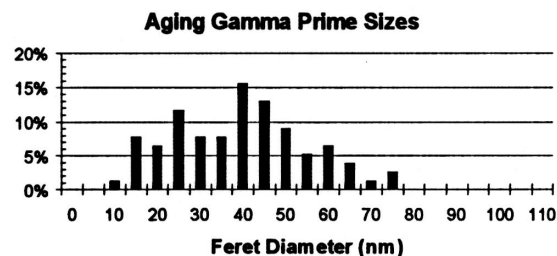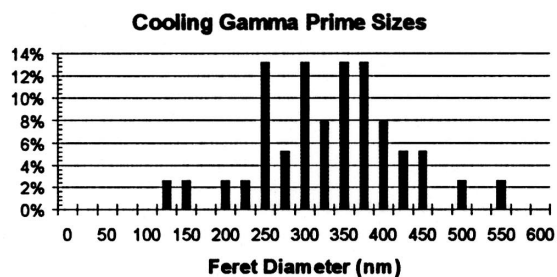
Figure 2(b).—γ' Feret diameter size distributions of KM4 ASTM 6.
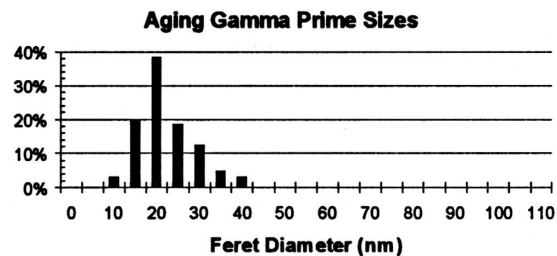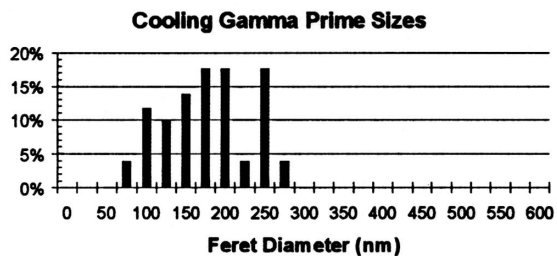
Figure 2(c).—γ' Feret diameter size distributions of KM4 ASTM 9.
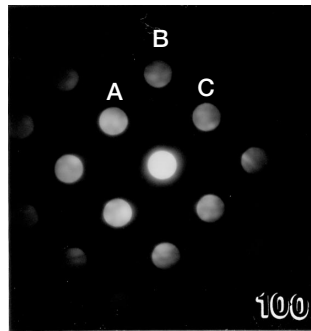
Figure 3(a).—MBED pattern for (Ti,Nb)C
carbides in KM4, [001] ZA, A = [020],
B = [220], C = [200].
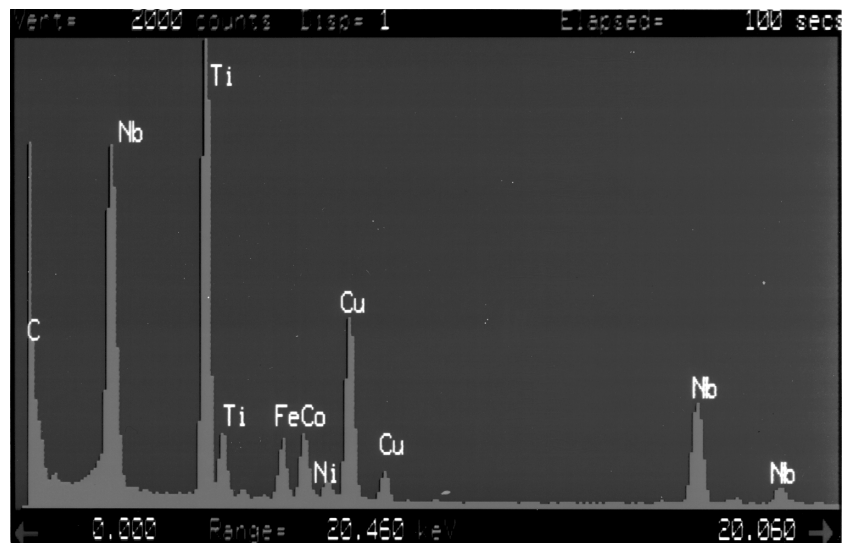
Figure 3(b).—Qualitative EDS spectrum for (Ti,Nb)C carbides in KM4.
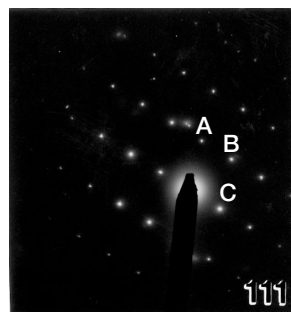
Figure 3(c).—SAD pattern for $(Mo,Cr)_3B_2$
borides in KM4, [111] ZA, A = $[0\bar{1}1]$,
B = $[\bar{1}01]$, C = $[\bar{1}10]$.
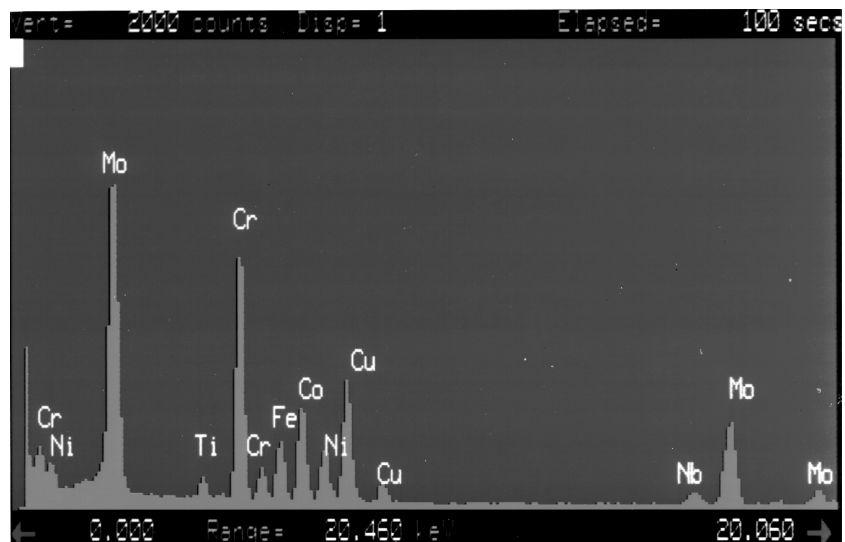
Figure 3(d).—Qualitative EDS spectrum for $(Mo,Cr)_3B_2$ borides in KM4.
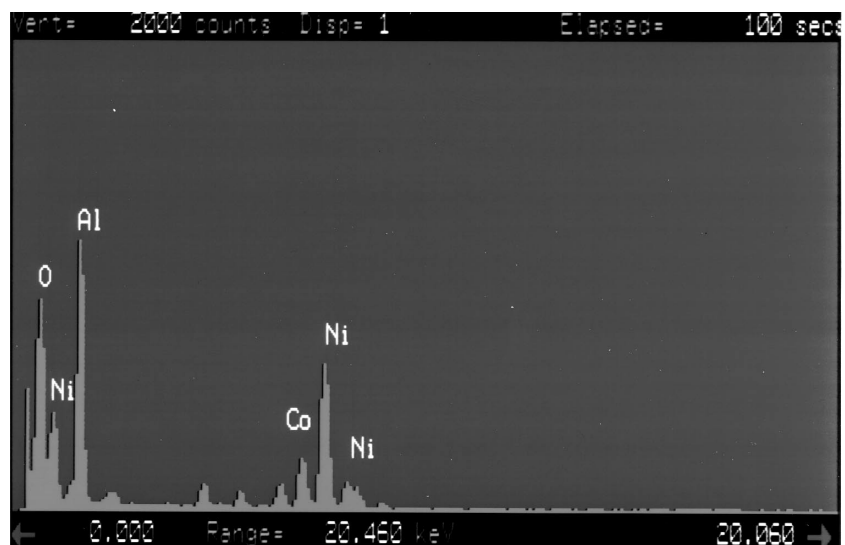
Figure 3(e).—Qualitative EDS spectrum for Al_2O_3 oxides in KM4.
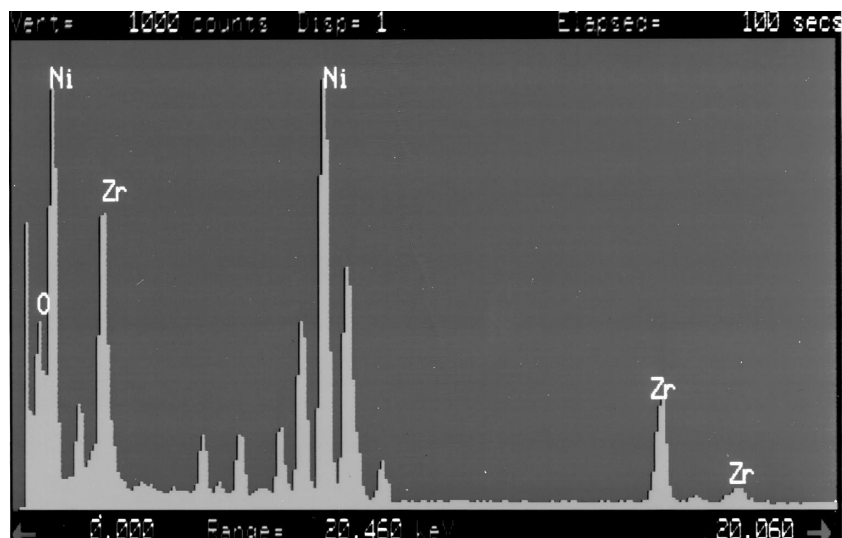
Figure 3(f).—Qualitative EDS pattern for ZrO_2 carbides in KM4.
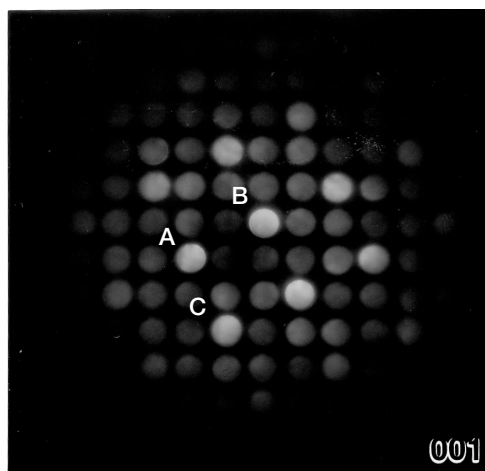
Figure 3(g).—SAD for $Cr_{23}C_6$ carbides in KM4, [001] Z.A.,
orientation relationship: [001]maxtrix ∥[001]carbides,
(100)matrix∥ (310)carbide, A [220]m, [8$\bar{4}$0]c; B [200]m,
[620]c; C [020]m, [2$\bar{6}$0]c.
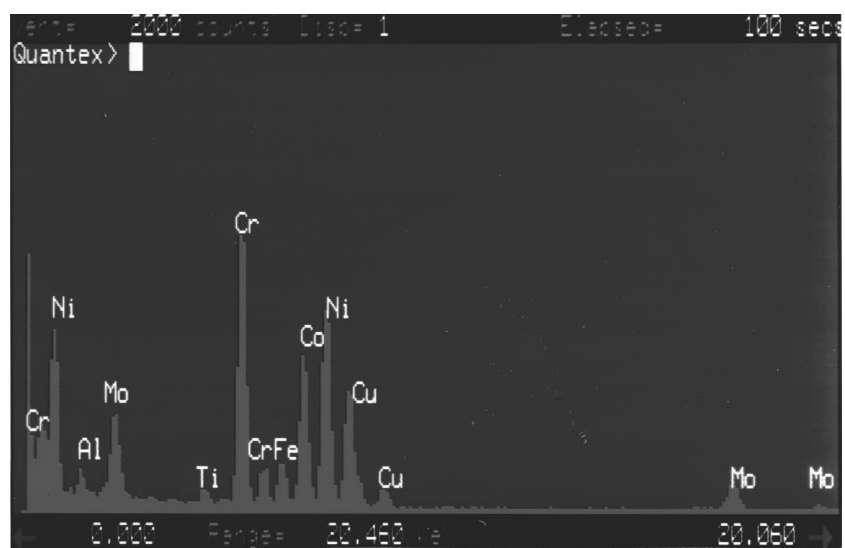
Figure 3(h).—Qualitative EDS pattern for $Cr_{23}C_6$ carbides in KM4.
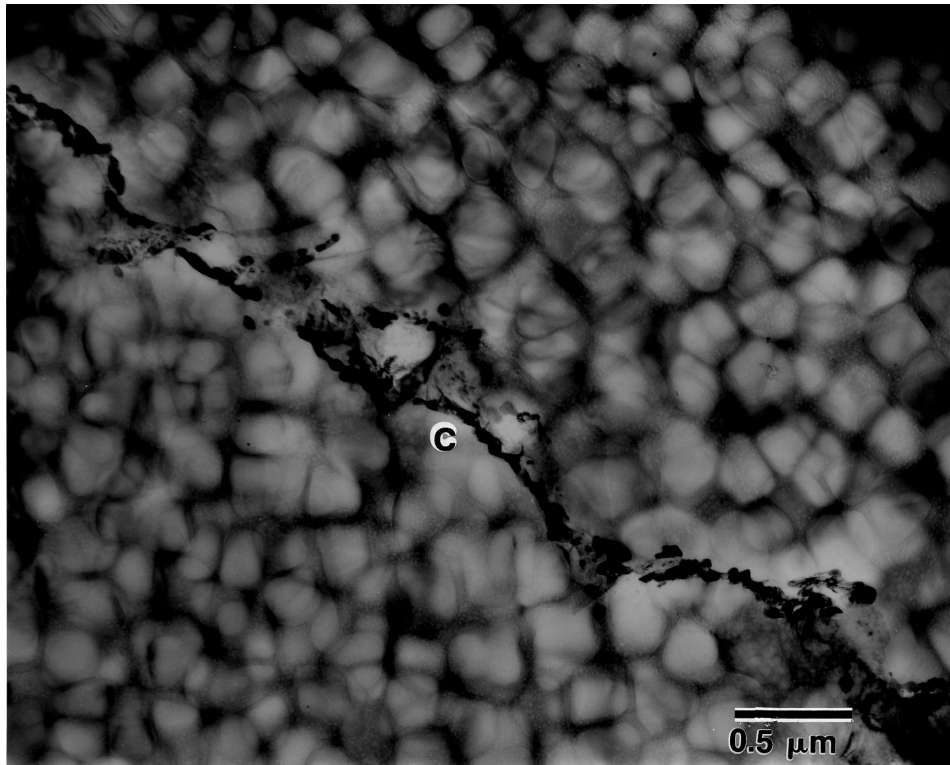
Figure 4(a).—TEM micrograph of KM4 ASTM 3 grain boundaries with a high frequency of carbides (C = $Cr_{23}C_6$).
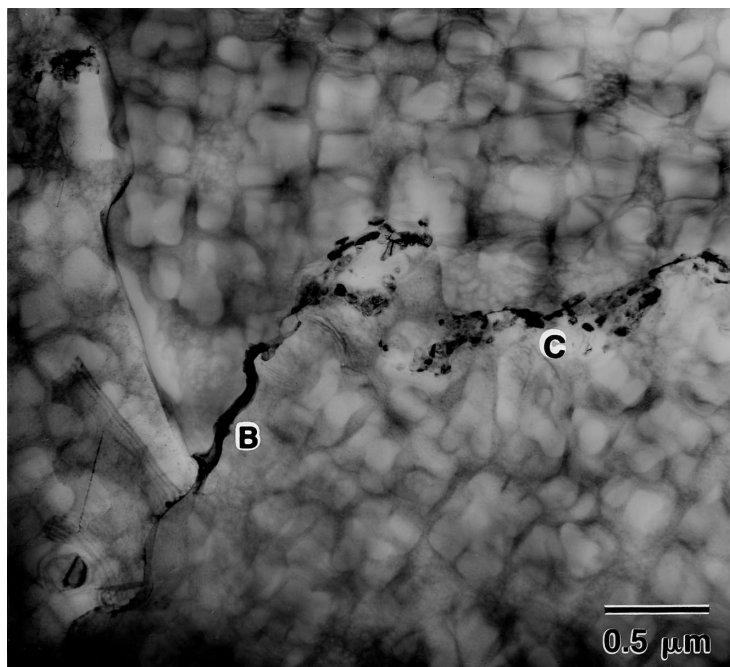
Figure 4(b).—TEM micrograph of KM4 ASTM 3 grain boundaries with a high frequency of carbides (B = $(Mo,Cr)_3B_2$, C = $Cr_{23}C_6$).

Figure 4(c).—TEM micrograph of typical KM4 ASTM 9 grain boundaries.
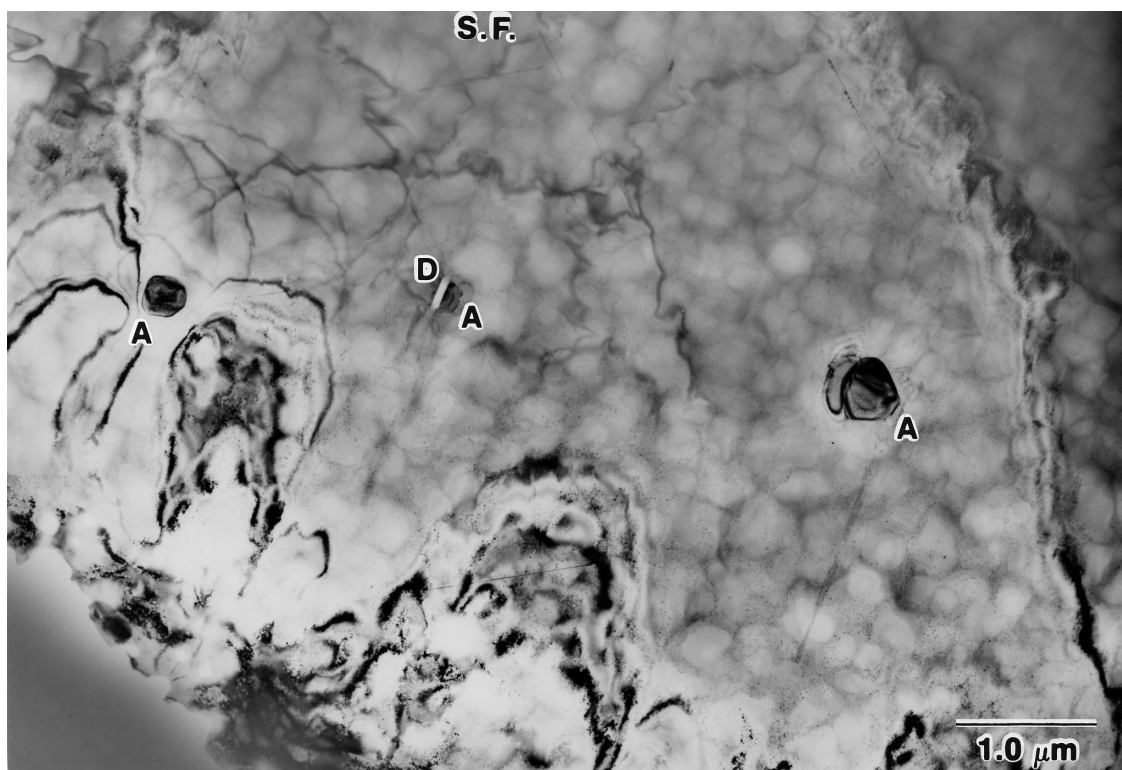
Figure 5(a).—Typical TEM micrograph showing general microstructure of CH98 ASTM 6, (A = (Ta,Ti)C, D = Al_2O_3; S.F. = stacking fault).
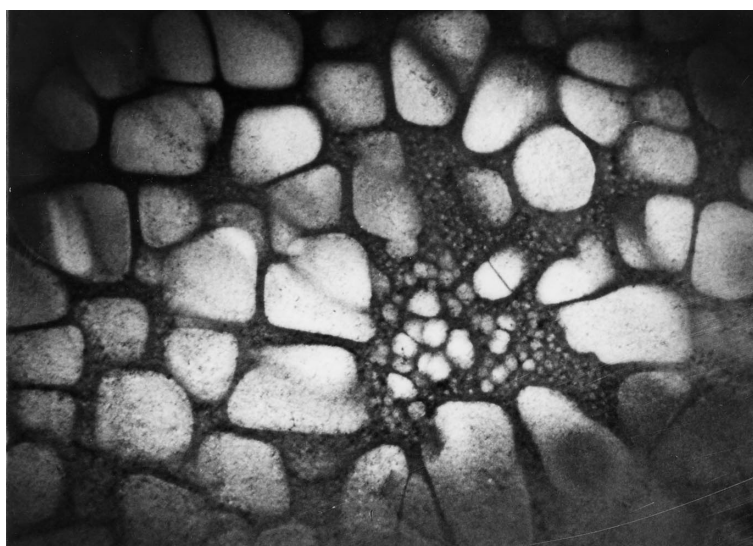
Figure 5(b).—Typical TEM micrograph showing γ' distribution of CH98.

Cooling Gamma Prime Sizes
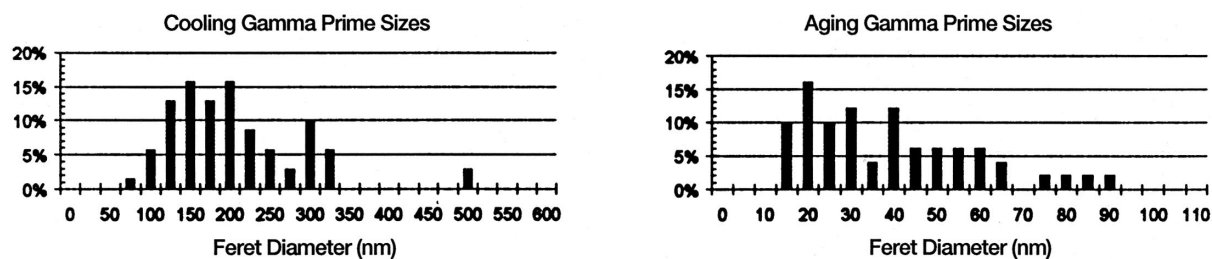
Figure 6.—γ' Feret diameter size distributions of CH98.
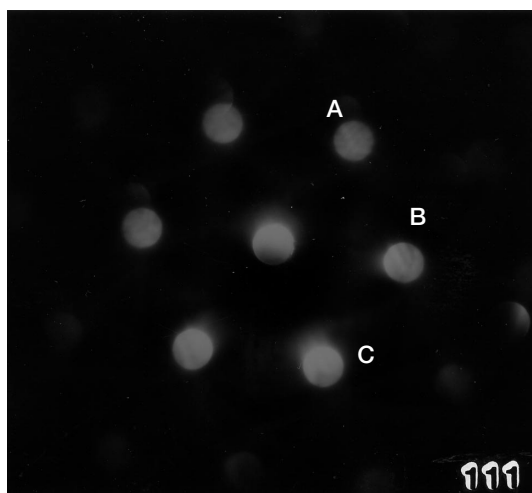
Figure 7(a).—MBED pattern of (Ta,Ti)C carbides in CH98, [111] Z.A., A [$\bar{2}$20], B [02$\bar{2}$], C [20$\bar{2}$].
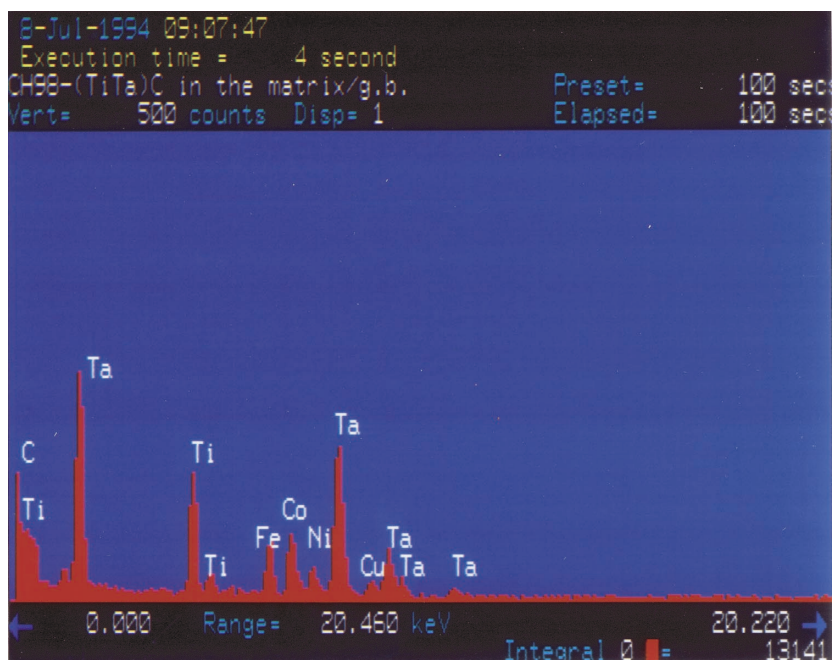
Figure 7(b).—Qualitative EDS spectrum for (Ta,Ti)C carbides in CH98.
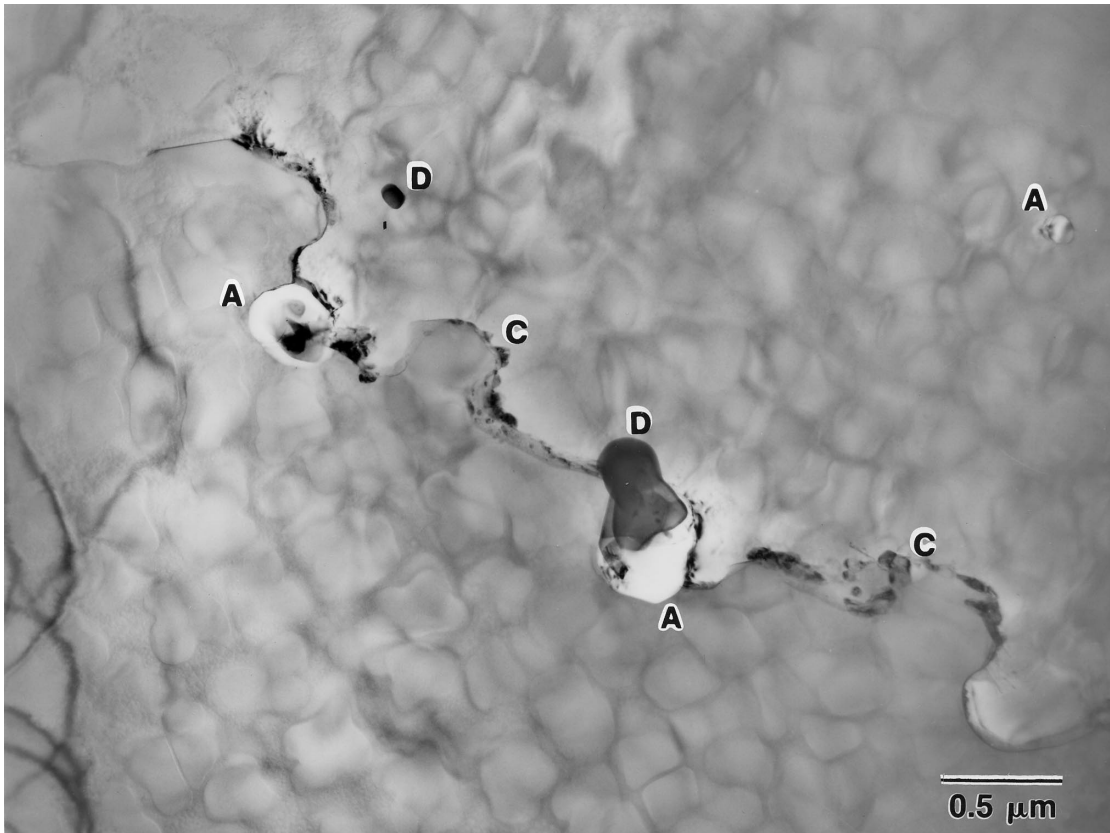
Figure 8.—Typical CH98 grain boundaries (A = (Ta,Ti)C, C = $Cr_{23}C_6$, D = Al_2O_3).
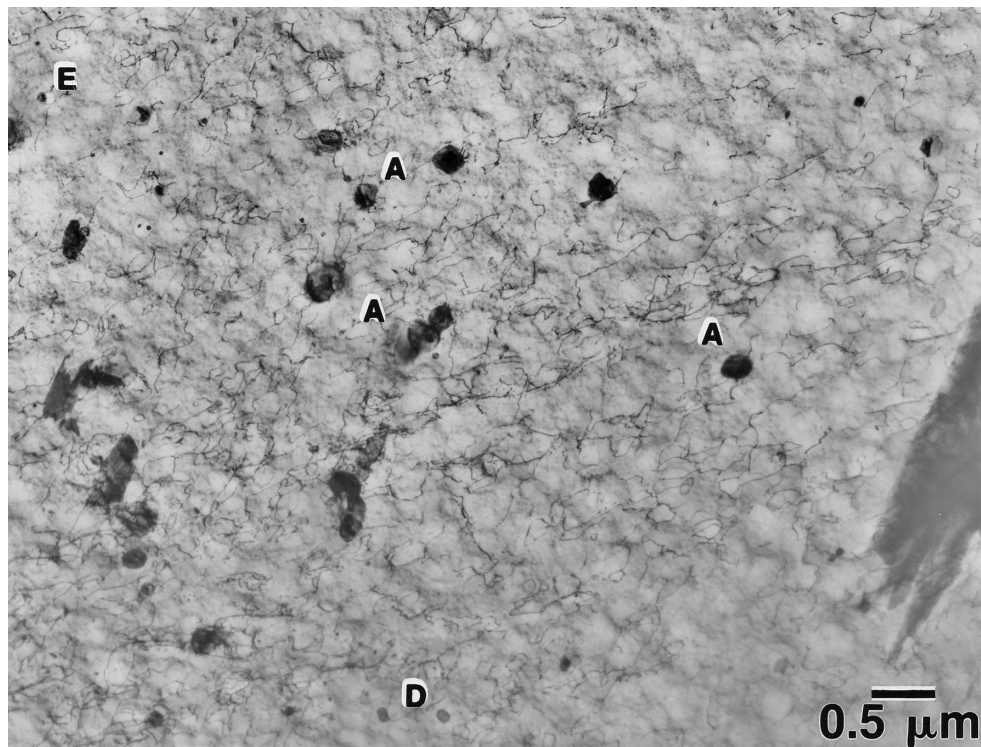
Figure 9(a).—Typical TEM micrograph showing general microstructure of René 88 DT (A = (Ti,Nb)C, D = Al$_2$O$_3$, E = ZrO$_2$).
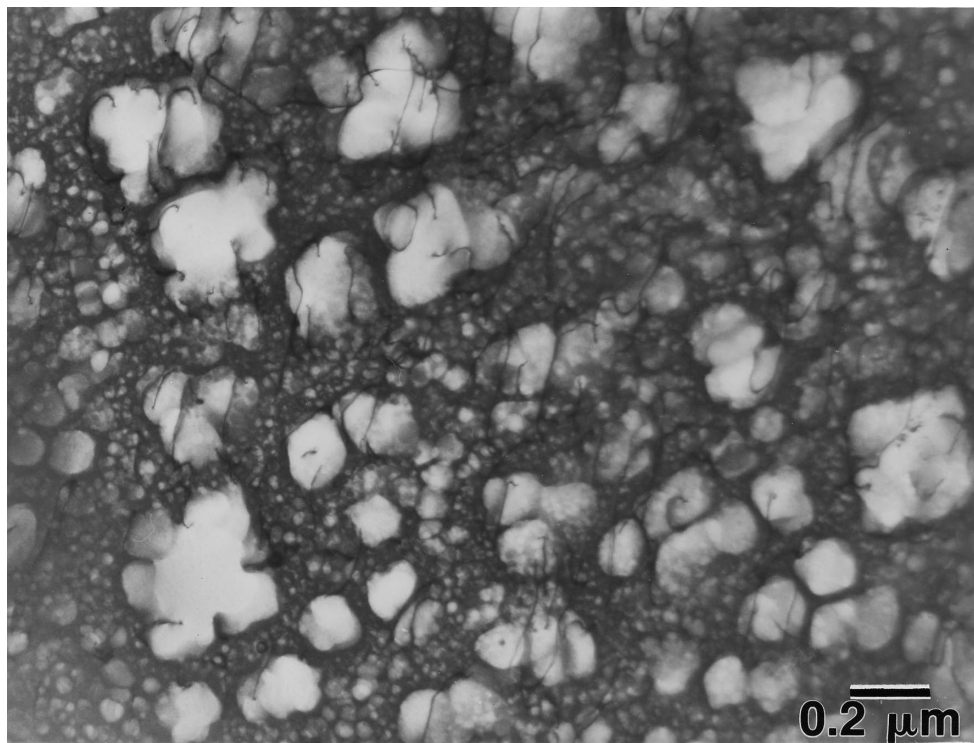
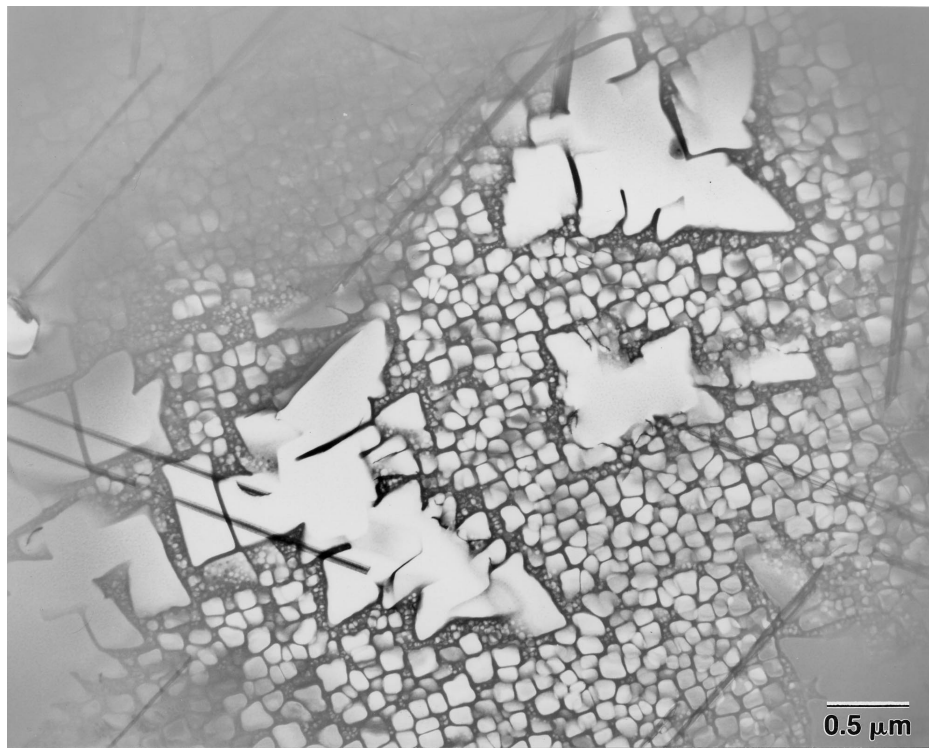**Figure 9(b).—Typical TEM micrograph of γ' distribution of René 88 DT.**
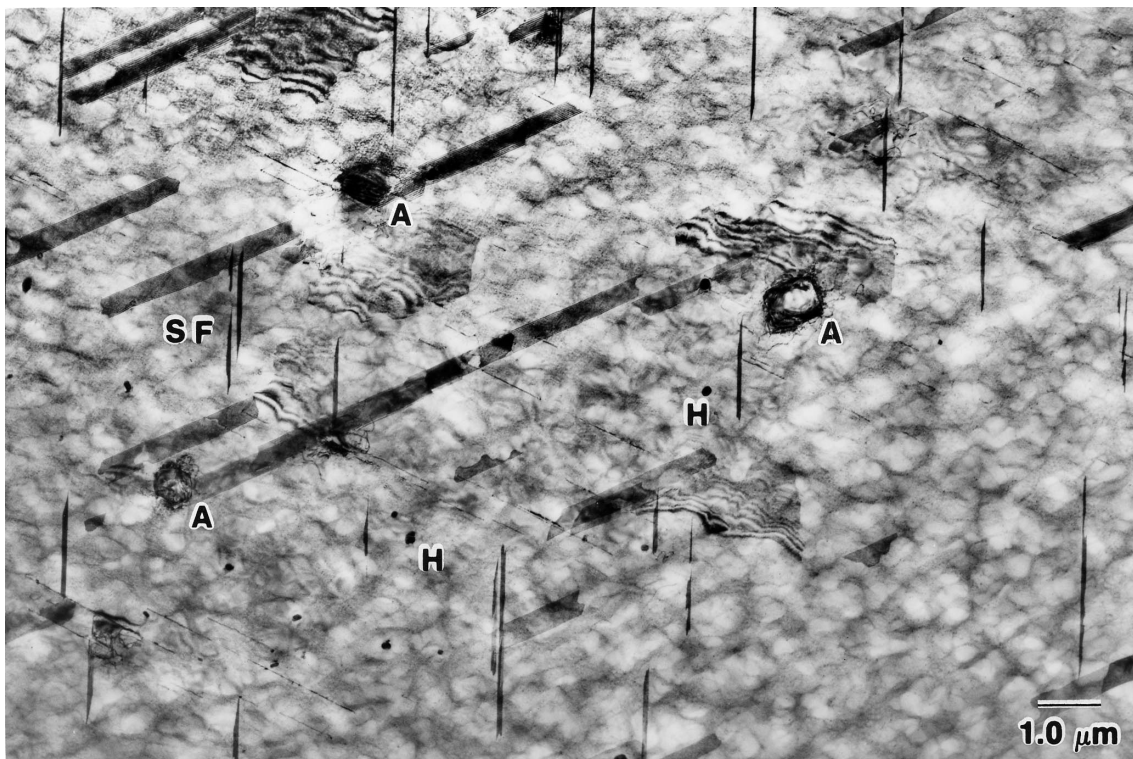
Figure 9(c).—Typical TEM micrograph showing general microstructure of SR3
(A = (Ti,Nb)C, H = $(Hf,Zr)O_2$, S.F. = stacking fault).
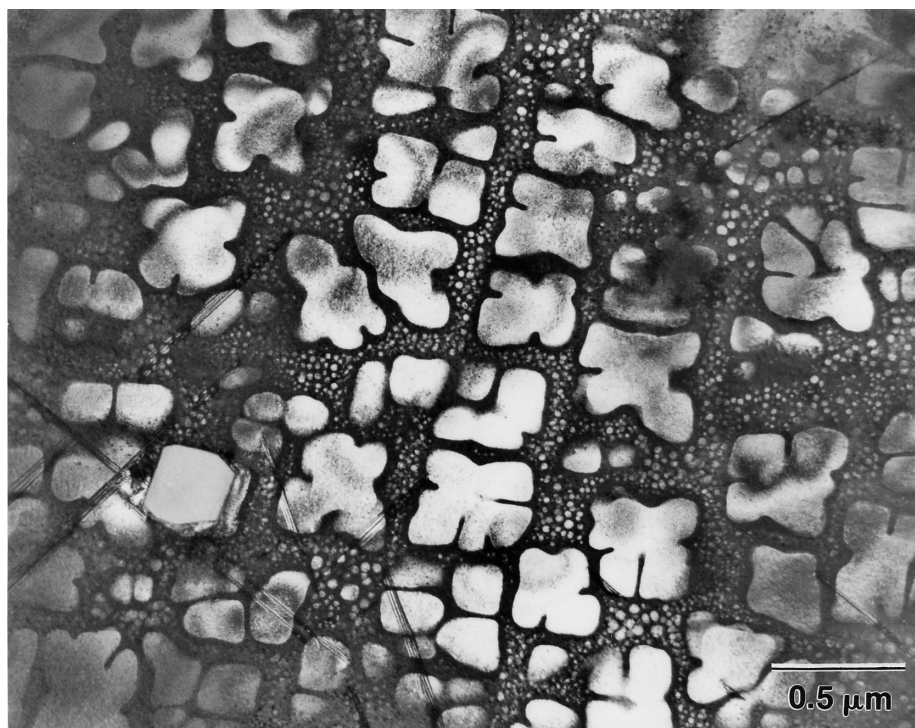
Figure 9(d).—Typical TEM micrograph of γ' distribution of SR3.
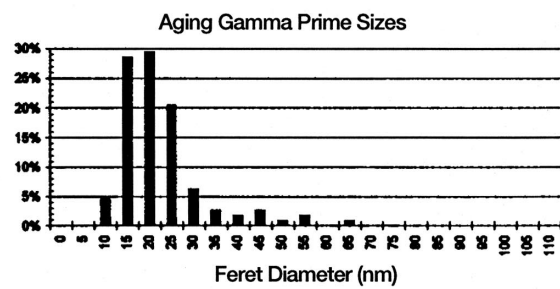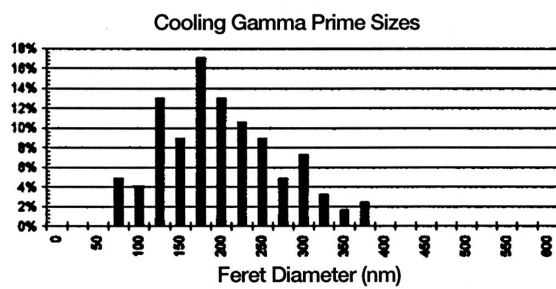
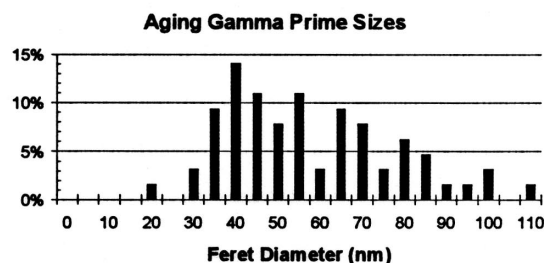Figure 10(a).—γ' Feret diameter size distributions of René 88 DT.
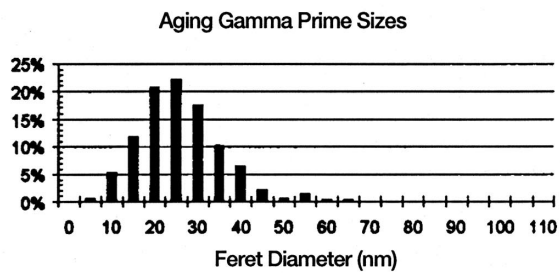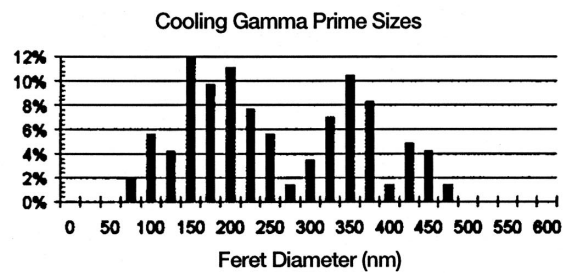
Figure 10(b).—γ' Feret diameter size distributions of SR3.
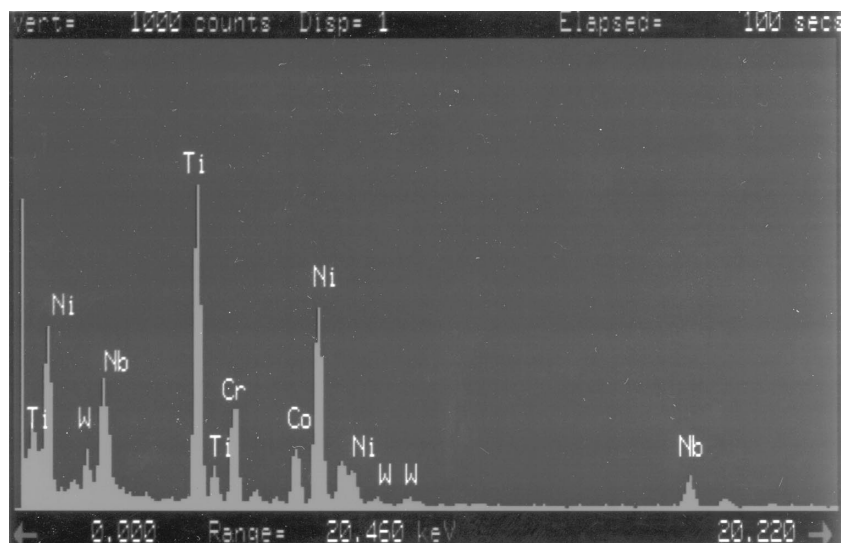
Figure 11(a).—Qualitative EDS spectrum of (Ti,Nb)C in René 88 DT.
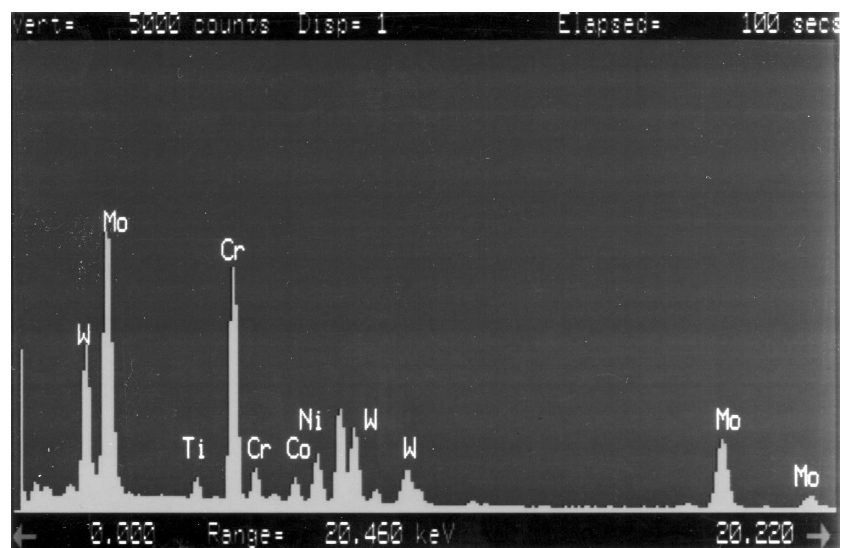
Figure 11(b).—Qualitative EDS spectrum of (Mo,Cr)$_3$B$_2$ in René 88 DT.
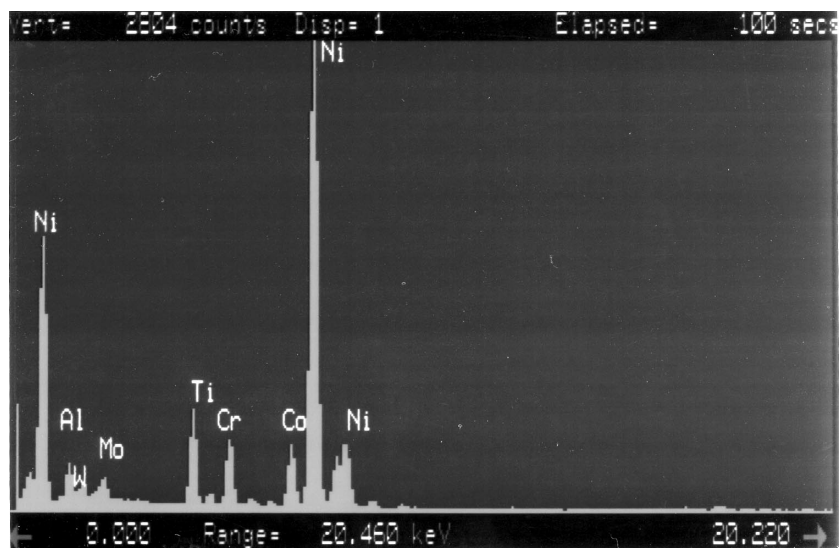
Figure 11(c).—Qualitative EDS spectrum of $(Ti,Mo)_6C$ in René 88 DT.
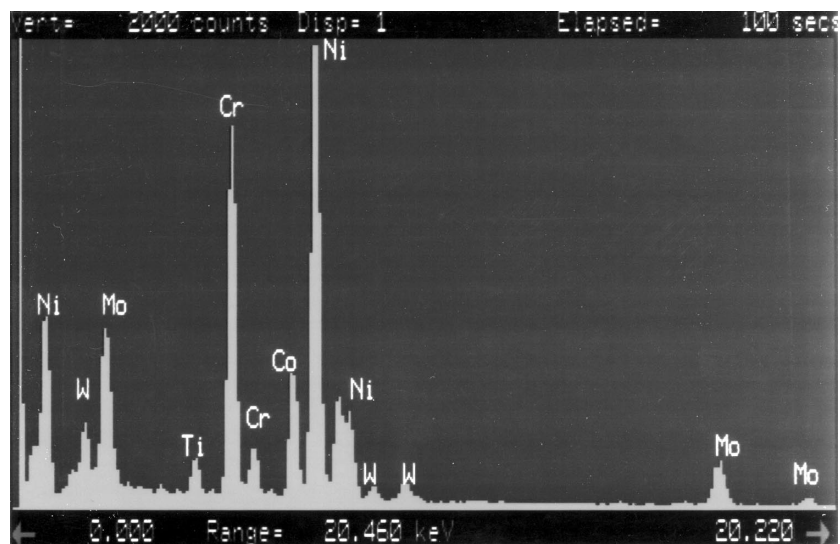
Figure 11(d).—Qualitative EDS spectrum of $Cr_{23}C_6$ in René 88 DT.
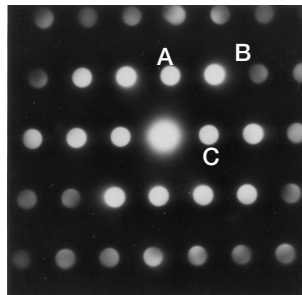
Figure 12(a).—MBED pattern of (Hf,Zr)O$_2$ oxides
in SR3, [011] Z.A., A [0$\bar{1}$1], B [1$\bar{1}$1], C [100].
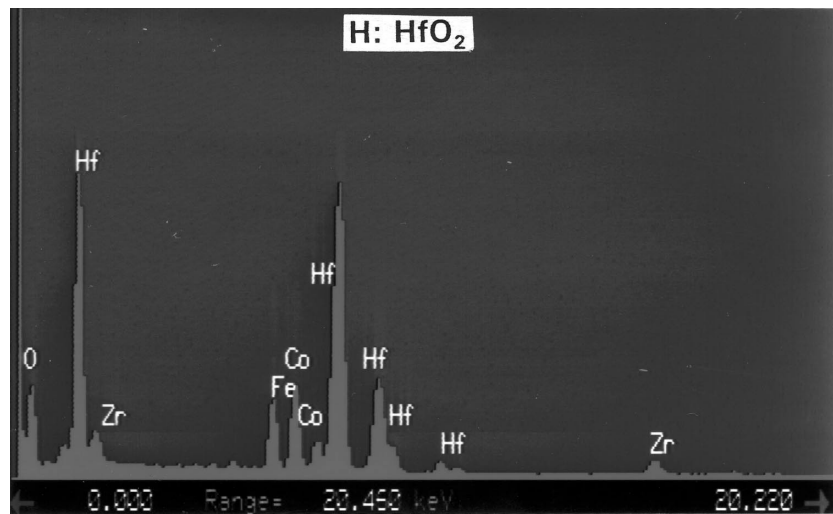
Figure 12(b).—Qualitative EDS spectrum for (Hf,Zr)O$_2$ oxides in SR3.
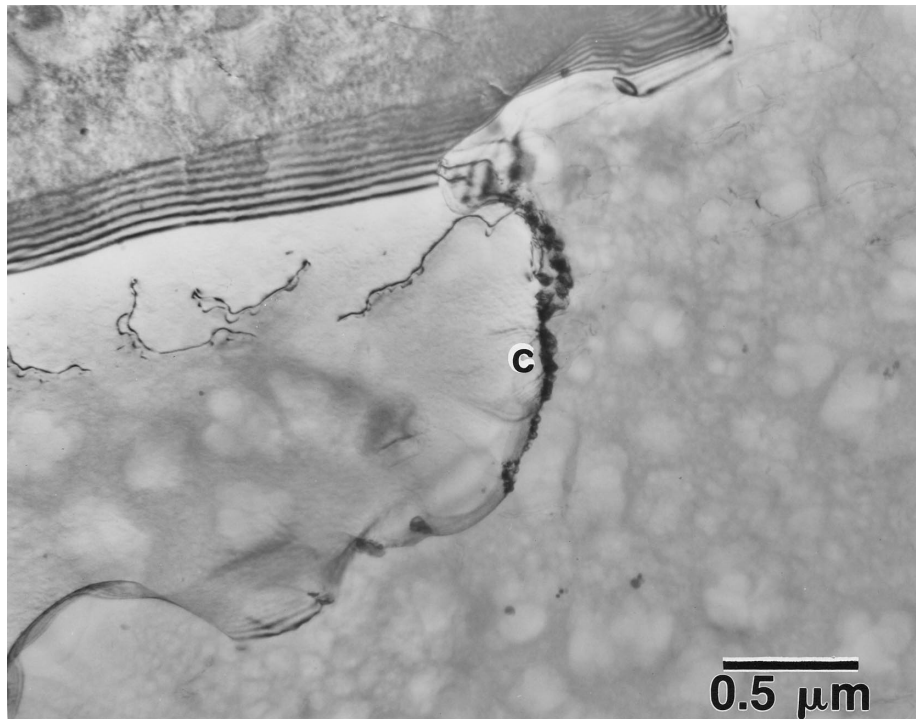
Figure 13(a).—TEM micrograph of typical René 88 DT grain boundaries with a high frequency of carbides (C = $Cr_{23}C_6$).
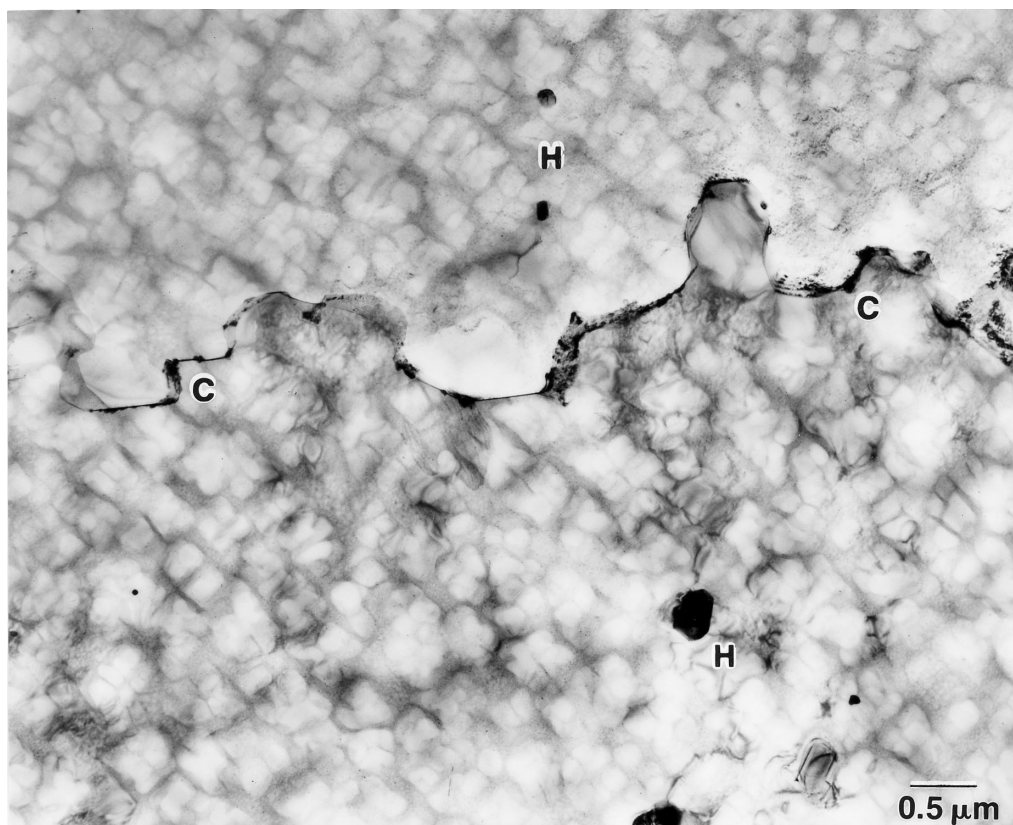
Figure 13(b).—TEM micrograph of typical SR3 grain boundaries with a high frequency of carbides (C = $Cr_{23}C_6$, H = $(Hf,Zr)O_2$).
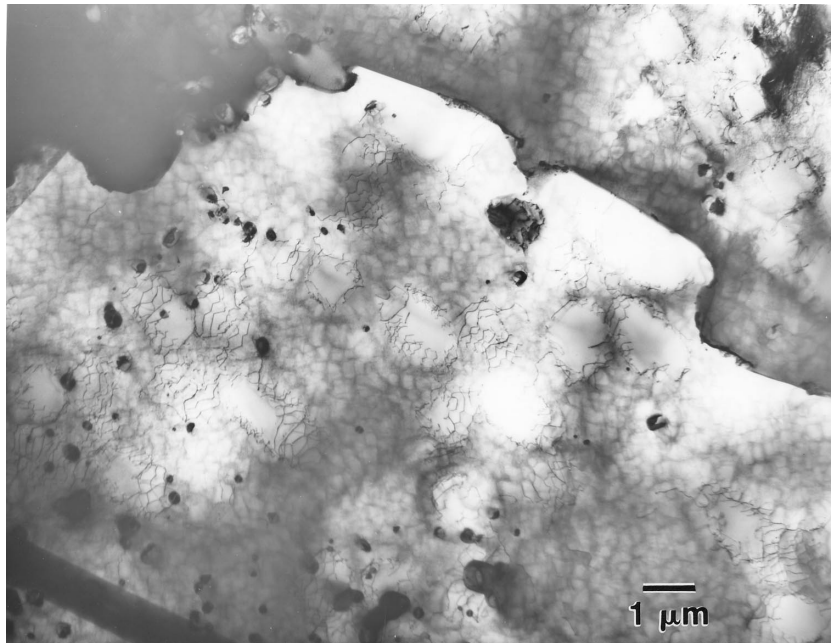
Figure 14(a).—Typical TEM micrograph showing general microstructure of IN-100.
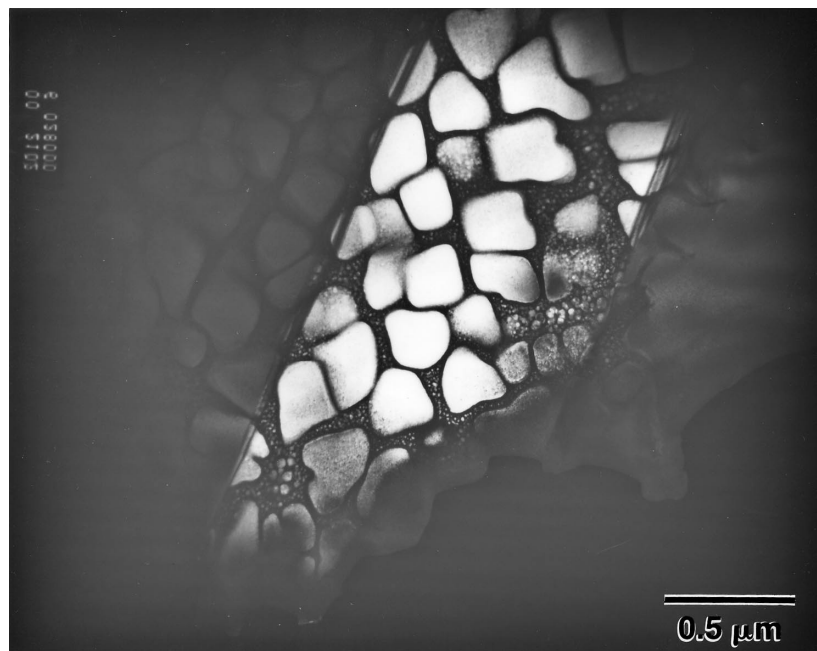
Figure 14(b).—Typical TEM micrograph showing cooling and aging γ' distribution of IN-100.
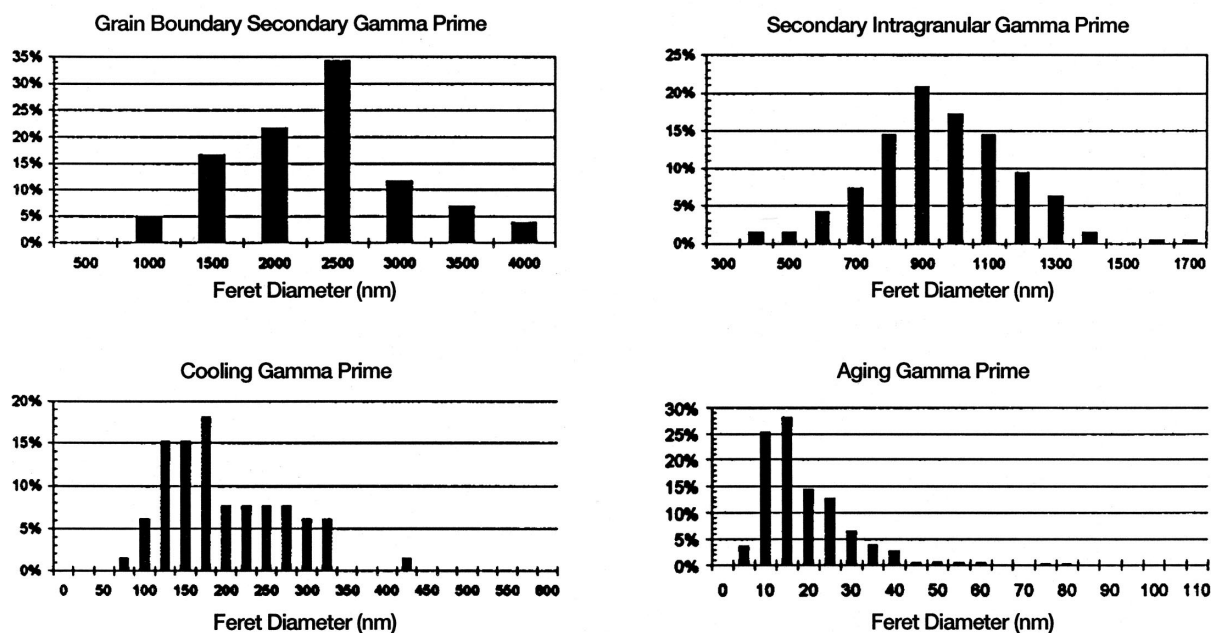
Figure 15(a).—γ' Feret diameter size distributions of IN-100.
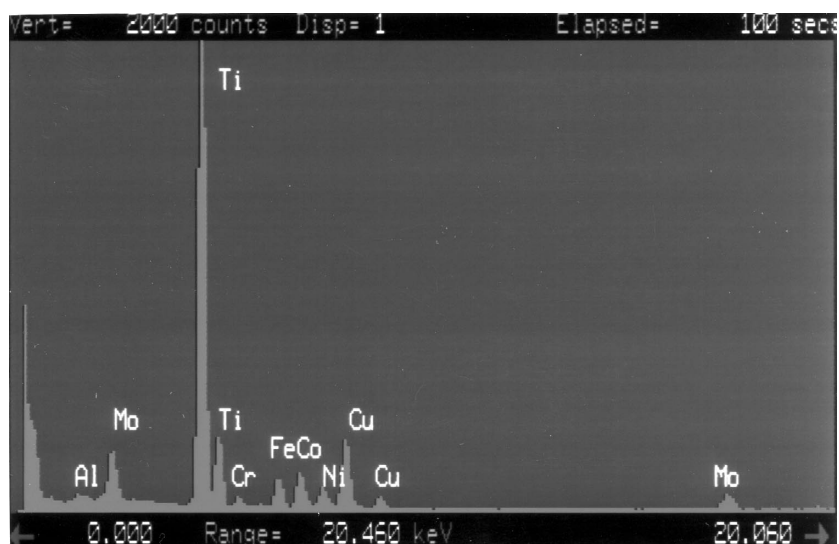
Figure 16.—Qualitative EDS spectrum of TiC carbides in IN-100.
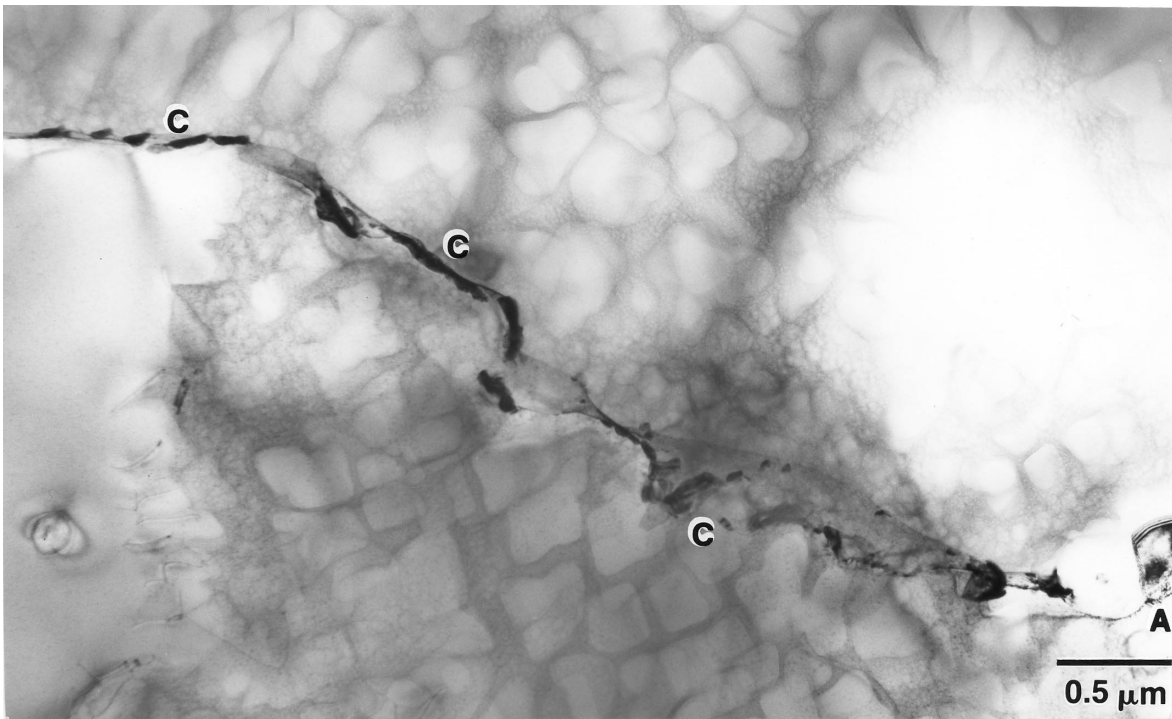
Figure 17.—TEM micrograph of typical IN-100 grain boundaries with a high frequency of carbides ($C = Cr_{23}C_6$).
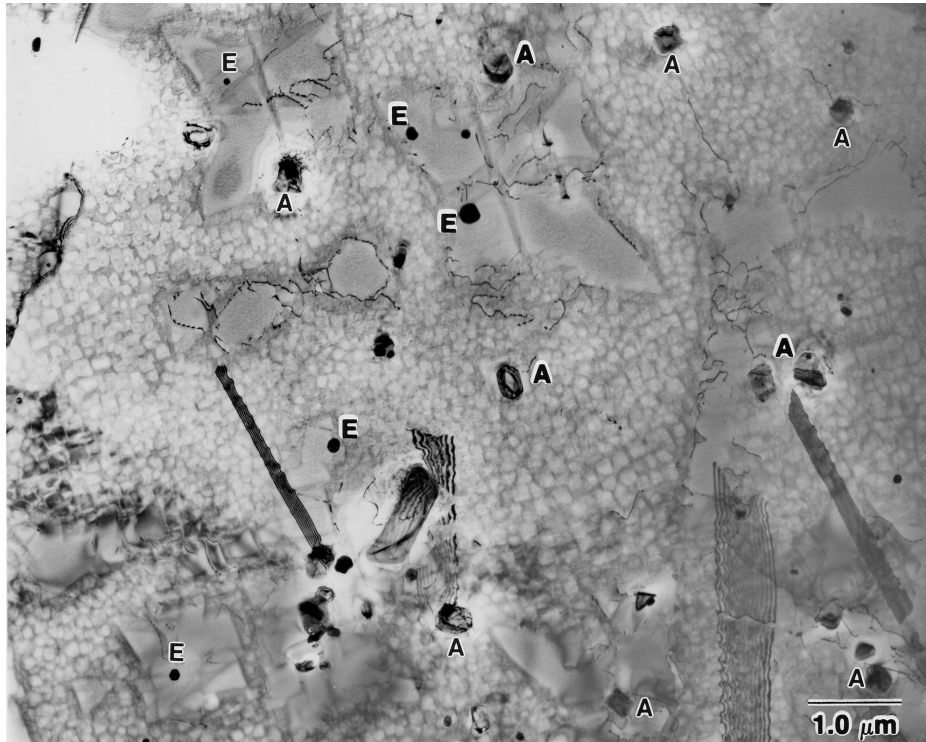
Figure 18(a).—Typical TEM micrograph showing general microstructure of 456-SC (A = (Ti,Nb)C, E = ZrO_2).

Figure 18(b).—Typical TEM micrograph showing γ' distribution of 456-SC.
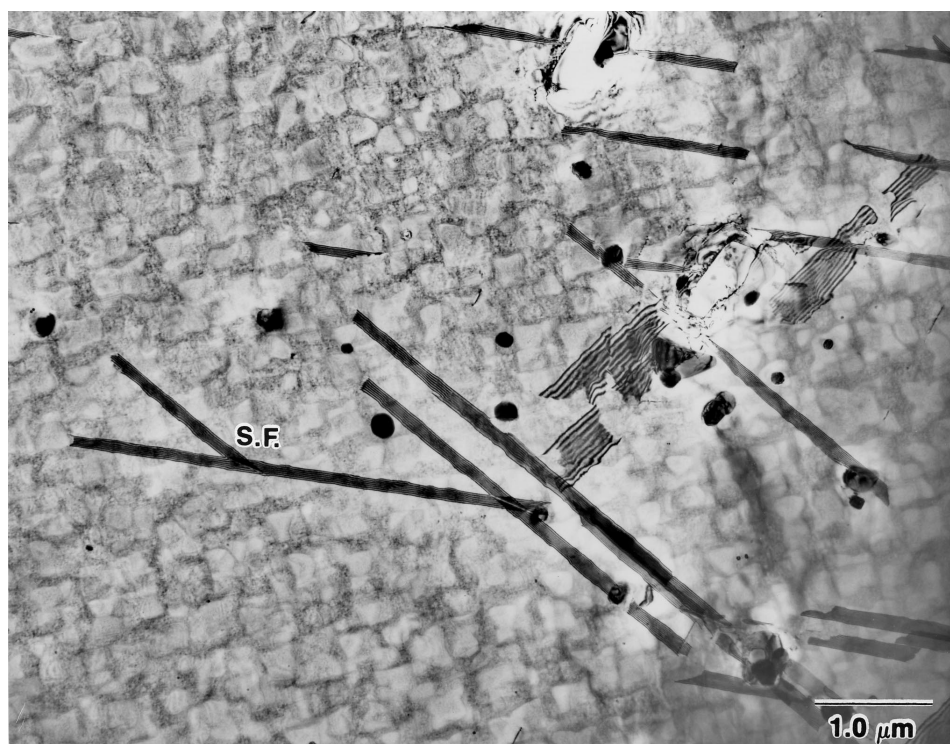
Figure 18(c).Typical TEM micrograph showing general microstructure of 456-FC (S.F. = stacking fault).
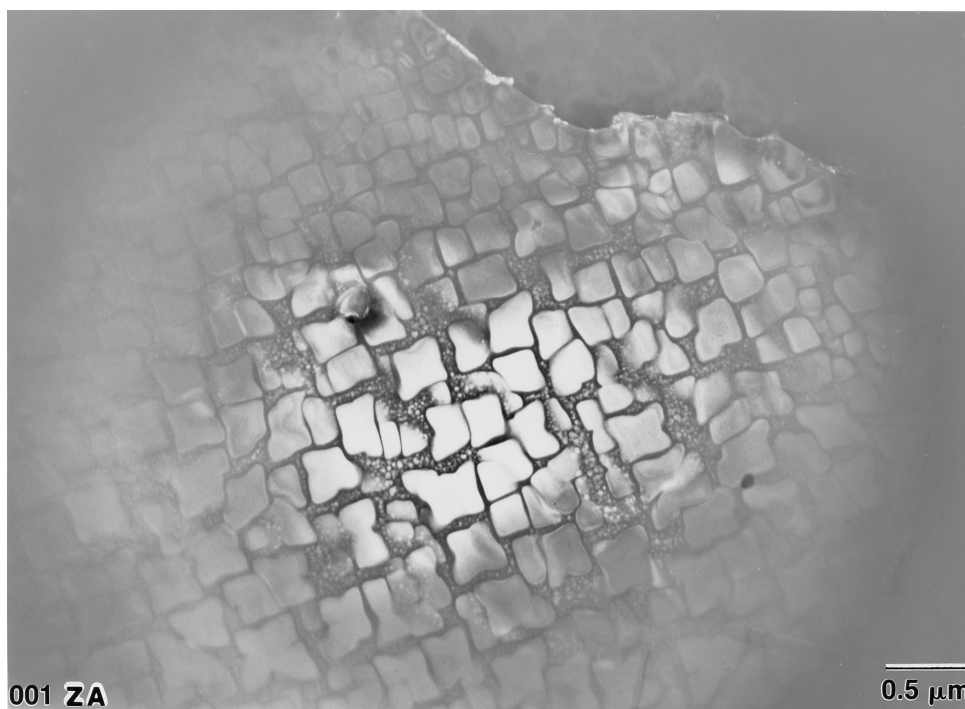
Figure 18(d).—Typical TEM micrograph showing γ' distribution of 456-FC.
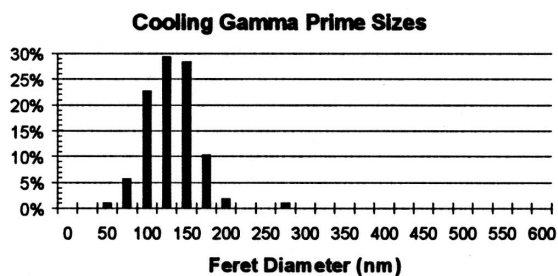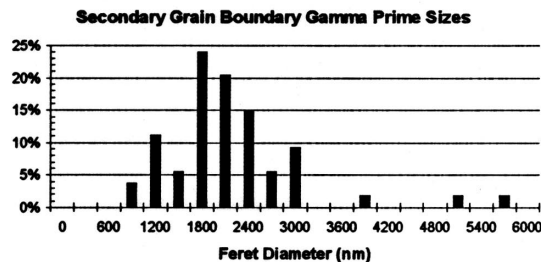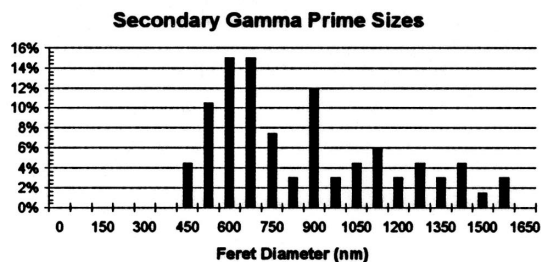
Figure 19(a).—γ' Feret diameter size distributions of 456-SC.
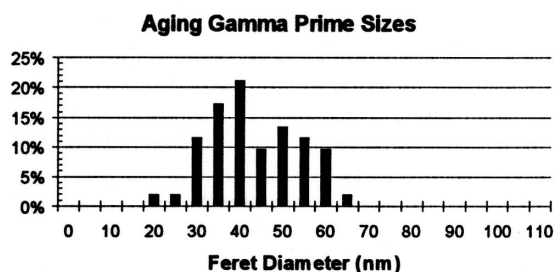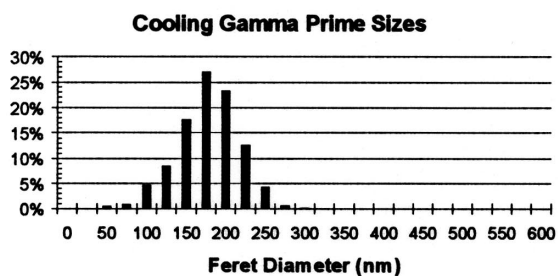

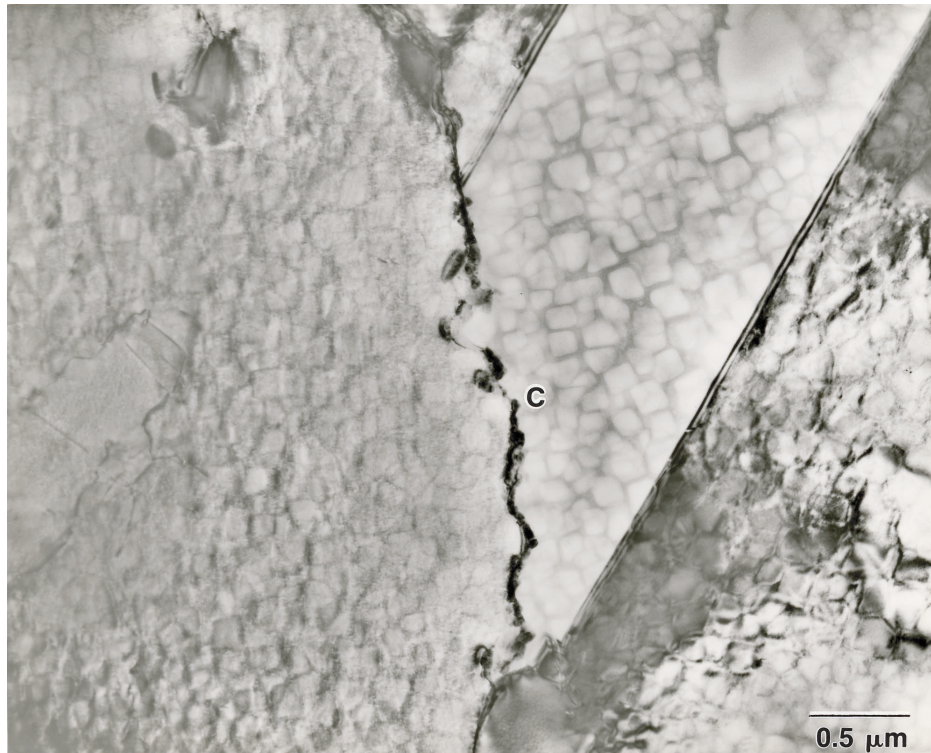Figure 19(b).—γ' Feret diameter size distributions of 456-FC.

Figure 20(a).—TEM micrograph of typical 456-SC grain boundaries with a high frequency of carbides (C = $Cr_{23}C_6$).
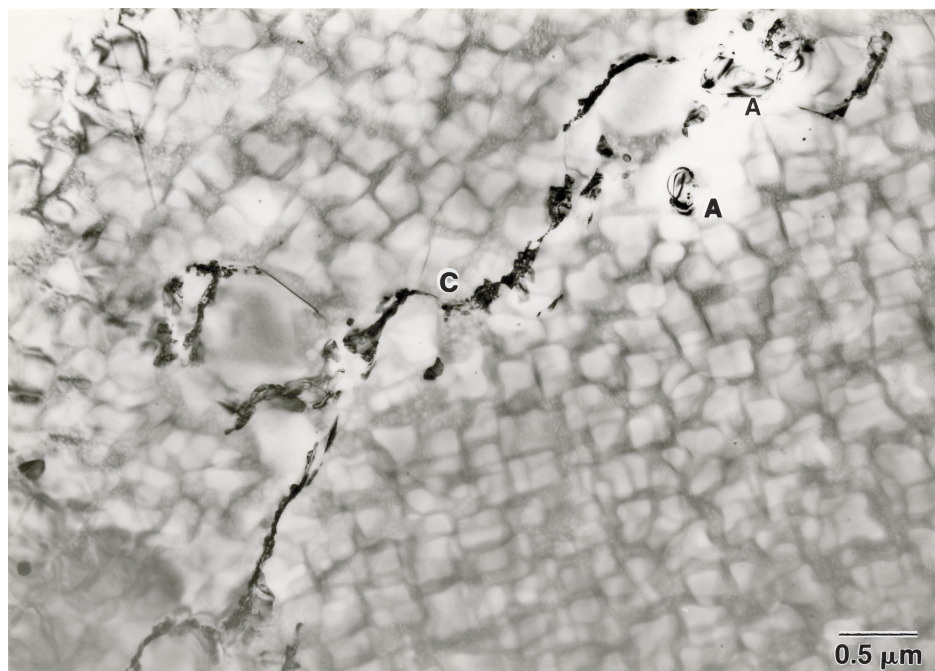

Figure 20(b).—TEM micrograph of typical 456-FC grain boundaries with a high frequency of carbides (A = (Ti,Nb)C, (C = $Cr_{23}C_6$).
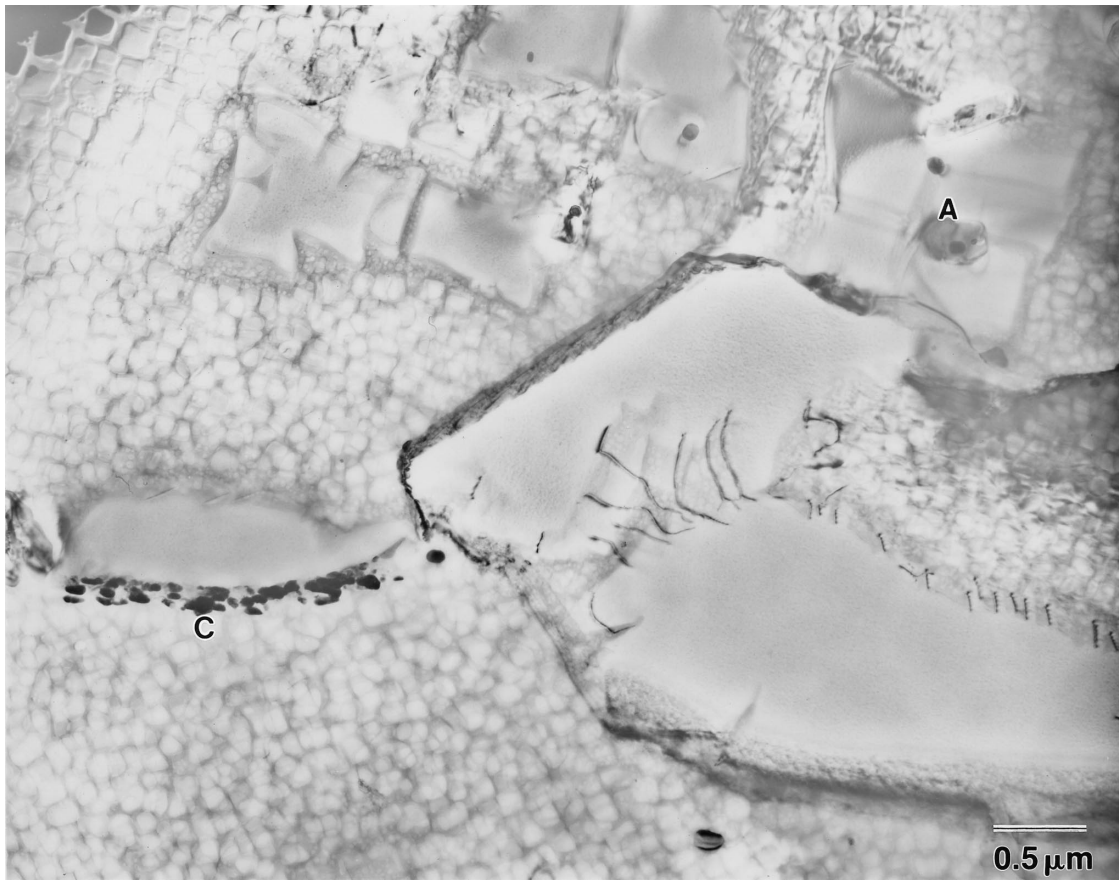
Figure 21.—Three grain boundaries in 456-SC showing three different carbide densities (A = (Ti,Nb)C, C = (C - $Cr_{23}C_6$).

REPORT DOCUMENTATION PAGE

Public reporting burden for this collection of information is estimated to average 1 hour per response, including the time for reviewing instructions, searching existing data sources, gathering and maintaining the data needed, and completing and reviewing the collection of information. Send comments regarding this burden estimate or any other aspect of this collection of information, including suggestions for reducing this burden, to Washington Headquarters Services, Directorate for Information Operations and Reports, 1215 Jefferson Davis Highway, Suite 1204, Arlington, VA 22202-4302, and to the Office of Management and Budget, Paperwork Reduction Project (0704-0188), Washington, DC 20503.

1. AGENCY USE ONLY (Leave blank)	2. REPORT DATE	3. REPORT TYPE AND DATES COVERED
	August 2004	Technical Memorandum

4. TITLE AND SUBTITLE

Microstructural Evaluations of Baseline HSR/EPM Disk Alloys

5. FUNDING NUMBERS

WBS–22–714–09–46

6. AUTHOR(S)

Timothy P. Gabb, Anita Garg, and David L. Ellis

7. PERFORMING ORGANIZATION NAME(S) AND ADDRESS(ES)

National Aeronautics and Space Administration
John H. Glenn Research Center at Lewis Field
Cleveland, Ohio 44135–3191

8. PERFORMING ORGANIZATION REPORT NUMBER

E–14617

9. SPONSORING/MONITORING AGENCY NAME(S) AND ADDRESS(ES)

National Aeronautics and Space Administration
Washington, DC 20546–0001

10. SPONSORING/MONITORING AGENCY REPORT NUMBER

NASA TM—2004-213123

11. SUPPLEMENTARY NOTES

12a. DISTRIBUTION/AVAILABILITY STATEMENT

Unclassified - Unlimited
Subject Category: 26   Distribution: Nonstandard

Available electronically at http://gltrs.grc.nasa.gov

This publication is available from the NASA Center for AeroSpace Information, 301–621–0390.

12b. DISTRIBUTION CODE

13. ABSTRACT (Maximum 200 words)

Six alloys representing two classes of powder metallurgy nickel-based superalloys were examined by transmission electron microscopy (TEM) and phase extraction. Alloys KM4, CH98, IN–100 and 456 are based on a Ni-18Co-12Cr composition while alloys René 88 DT and SR 3 have lower Al and Co and higher Cr contents. The γ' size distributions were determined from quantitative image analysis of the TEM images. The volume fraction of γ' and carbides and the composition of the phases were determined by a combination of phase extraction and TEM. The results showed many similarities in γ' size distributions, grain boundary serrations, and grain boundary carbide frequencies between alloys KM4, CH98, 456, René 88 DT and SR 3 when heat treated to give an approximate grain size of ASTM 6. The density of grain boundary carbides in KM4 was shown to substantially increase as the grain size increased. IN–100 and 456 subjected to a serration cooling heat treatment had much more complex γ' size distributions with very large inter-granular and intragranular secondary γ' as well as finer than average cooling and aging γ'. The grain boundary carbides in IN–100 were similar to the other alloys, but 456 given the serration cooling heat treatment had a more variable density of grain boundary carbides. Examination of the phases extracted from the matrix showed that there were significant differences in the phase chemistries and elemental partitioning ratios between the various alloys.

14. SUBJECT TERMS

Superalloy, Disk; Turbine

15. NUMBER OF PAGES
60

16. PRICE CODE

17. SECURITY CLASSIFICATION OF REPORT	18. SECURITY CLASSIFICATION OF THIS PAGE	19. SECURITY CLASSIFICATION OF ABSTRACT	20. LIMITATION OF ABSTRACT
Unclassified	Unclassified	Unclassified	

NSN 7540-01-280-5500

Standard Form 298 (Rev. 2-89)
Prescribed by ANSI Std. Z39-18
298-102